



## 저작자표시-비영리-변경금지 2.0 대한민국

이용자는 아래의 조건을 따르는 경우에 한하여 자유롭게

- 이 저작물을 복제, 배포, 전송, 전시, 공연 및 방송할 수 있습니다.

다음과 같은 조건을 따라야 합니다:



저작자표시. 귀하는 원저작자를 표시하여야 합니다.



비영리. 귀하는 이 저작물을 영리 목적으로 이용할 수 없습니다.



변경금지. 귀하는 이 저작물을 개작, 변형 또는 가공할 수 없습니다.

- 귀하는, 이 저작물의 재이용이나 배포의 경우, 이 저작물에 적용된 이용허락조건을 명확하게 나타내어야 합니다.
- 저작권자로부터 별도의 허가를 받으면 이러한 조건들은 적용되지 않습니다.

저작권법에 따른 이용자의 권리는 위의 내용에 의하여 영향을 받지 않습니다.

이것은 [이용허락규약\(Legal Code\)](#)을 이해하기 쉽게 요약한 것입니다.

[Disclaimer](#)

공학석사 학위논문

# Investigation of crystallographic structures and defects in $\text{WSe}_2$ spiral pyramid

나선 피라미드형 이셀레늄화텅스텐의 결정 구조와  
결함 분석

2023년 2월

서울대학교 대학원

공과대학 재료공학부

이 주 상

# Investigation of crystallographic structures and defects in WSe<sub>2</sub> spiral pyramid

지도 교수 김 미 영

이 논문을 공학석사 학위논문으로 제출함  
2022년 12월

서울대학교 대학원  
공과대학 재료공학부  
이 주 상

이주상의 공학석사 학위논문을 인준함  
2022년 12월

위 원 장 \_\_\_\_\_ 김 영 운 (인)

부위원장 \_\_\_\_\_ 김 미 영 (인)

위 원 \_\_\_\_\_ 이 관 형 (인)

# Abstract

## Investigation of crystallographic structures and defects in WSe<sub>2</sub> spiral pyramid

Jusang Lee

Department of Materials Science and Engineering

The Graduate School

Seoul National University

Spiral transition metal dichalcogenides are of great interest because they can be applied as nano size inductors or electrodes. In this study, tungsten diselenium (WSe<sub>2</sub>) is analyzed using a transmission electron microscope. A technique to identify defects in van der Waals materials and analyze the stacking method is presented. It will be helpful in analyzing the cause of device deterioration when using van der Waals materials in engineering.

Spiral WSe<sub>2</sub> forms a spiral dislocation at the center, and one face continuously grows spirally to take a pyramid shape. The screw dislocation in the center in the [0001] direction of the spiral WSe<sub>2</sub> crystal and the edge dislocation in the horizontal direction in the [10 $\bar{1}$ 0] direction are entangled and the edge dislocation is fixed at one position, so this region can be observed in detail. Using the fact that the dislocation contrast becomes zero when the inner product of the Burgers vector and the diffraction vector is zero, it was confirmed that the Burgers vector of the potential is in the

[1–210] direction.

In order to analyze the size of the Burgers vector, atomic resolution high angle annular dark field–scanning transmission electron microscope (HAADF–STEM) images were acquired. As a result, in the bilayer region, it was confirmed that the dislocation formed by shrinking the upper layer by one unit cell in [1–210] direction, and the Burgers vector was determined to be  $1/3$  [1–210].

In van der Waals materials, these dislocations can exist widely spread in the plane due to the weak interplanar interaction. The equilibrium dislocation width can be calculated by finding the balance point between the energy that becomes unstable due to interplanar stacking misalignment and the energy that is stabilized by spreading the strain field widely.

In addition, a 4-dimensional scanning transmission electron microscope image was obtained, which stores diffraction patterns at each scanning point as images. Among possible stacking sequences, the diffraction patterns for each tilt angle of the stacked structure corresponding to the 3R structure were simulated through the muSTEM program. Average intensity and polarity are defined as two factors that characterize the stacking order in the diffraction pattern. As for the average intensity, it was confirmed that when the thickness is 15 layers or less and the tilt angle  $\theta$  of the specimen was 10 mrad or less, the 3R structure rapidly darkened with a cycle of 3 layers. The polarity showed a phenomenon in which the sign is reversed when the stacking order is reversed. In

the case of the experimentally measured diffraction pattern, the sign of the left side and right side polarity was reversed through the edge dislocation. Even if the stacking order is not reversed, there may be other reasons why the sign of polarity is reversed, so further research is needed.

**Keyword :** Van der Waals materials, edge dislocation, staking sequence, transmission electron microscope, four dimensional scanning transmission electron microscopy

**Student Number :** 2019–26531

# Table of Contents

Abstract

Table of Contents

List of Figures

## Chapter 1. Introduction ..... 14

1.1. Van der Waals Materials

1.2. Structure of spiral TMD

1.3. Transmission electron microscopy analysis

1.3.1 High resolution transmission electron microscopy  
(HRTEM)

1.3.2. High angle annular dark field scanning transmission  
electron microscopy (HAADF STEM)

1.3.3. Dark field transmission electron microscopy (DFTEM)

1.3.4. 4 dimensional–scanning transmission electron microscopy  
(4D–STEM)

## Chapter 2. Exprimental Methods ..... 37

2.1. Synthesis of spiral WSe<sub>2</sub>

2.2. Specimen preparation and TEM analysis

2.3. TEM analysis

2.4. Electron diffraction simulation

2.5. Computational details

## **Chapter 3. Results and Discussion ..... 41**

3.1. Analysis of edge dislocation in bilayer  $\text{WSe}_2$

3.1.1. Determination of the number of  $\text{WSe}_2$  layers

3.1.2. Determination of the type of dislocation

3.1.3. Atomic resolution analysis of dislocation in bilayer  $\text{WSe}_2$

3.1.4. Formulation of dislocation energy in van der Waals bilayer structure

3.2. Determination of stacking order of multi layered  $\text{WSe}_2$

3.2.1. Bilayer binding energy of  $\text{WSe}_2$  and possible candidates for a stacking sequence in spiral  $\text{WSe}_2$

3.2.2. PACBED simulation for various stacking sequence of multilayer  $\text{WSe}_2$

3.2.3. Experimental 4D-STEM image of spiral  $\text{WSe}_2$

## **Chapter 4. Conclusions ..... 67**

## **Bibliography ..... 69**

## **Abstract in Korean..... 72**



## List of Figures

**Figure 1.** 2D materials library <sup>[1]</sup>. Blue shading indicates monolayers that have been proved to be stable at room temperature in air. Green shading indicates monolayers that are probably stable in air. Pink shading indicates monolayers that are unstable in air but may be stable in inert atmosphere. Grey shading indicates 3D compounds that have been successfully exfoliated down to monolayers.

**Figure 2.** Schematic illustrations of (a) conventional epitaxy in which misfit dislocations nucleate to mitigate the stress due to lattice mismatch, (b) van der Waals epitaxy in which both the films and the substrate have no dangling bonds, and (c) vdW epitaxy on a passivated conventional 3D substrate <sup>[2]</sup>.

**Figure 3.** Schematic illustration of building van der Waals heterostructures as building Lego blocks <sup>[1]</sup>. Conceptually, this atomic-scale Lego resembles molecular beam epitaxy but employs different construction rules and a distinct set of materials.

**Figure 4.** Growing mechanism of atomic layered MoS<sub>2</sub> spiral <sup>[4]</sup>. (a–d) Schematic illustration of MoS<sub>2</sub> spiral from nucleation to growth. Black lines indicate the exposed edges. (e–h) AFM images (phase signal) of several typical spirals at different growth stages. The growth will start from (e) a slipped edge and generate (f) a small

spiraled triangle. With growth continued, the generated dislocation core will keep spiraling up vertically and form (g,h) pyramid-shaped 3D large spirals.

**Figure 5.** (a) SEM image of the MoS<sub>2</sub> pyramid with a white rectangle where the cross-section cut was made. (b) Atomic resolution imaging of the layer stacking of MoS<sub>2</sub>.

**Figure 6.** Application of spiral TMD. (a) Schematic illustration of helical current of spiral MoS<sub>2</sub><sup>[5]</sup>. (b) Schematic illustration of electrochemical microcell assembly. WS<sub>2</sub> with many active sites is used as an electrode for hydrogen generation reaction<sup>[6]</sup>.

**Figure 7.** Crystal structures of the most common TMD polytypes: 2H(a, c; ICSD, 24000) and 3R(b, e; ICSD, 38401)<sup>[7]</sup>. (a, b) Crystals viewed along the a-axis, where the unit cell is shown as a grey box and 3R rhombohedral unit cell is shown as a red box. Layer directions shown by grey chevrons and layer names on the right. (c, d) Bilayers viewed along the c-axis.

**Figure 8.** Two WSe<sub>2</sub> monolayer which is antiparallel. The atoms on the edge sites are indicated. Each layer can be overlapped to the other when the layer is rotated by 60° or 180°.

**Figure 9.** Screw dislocation growth diagrams<sup>[7]</sup>. (a) side on (a-axis) model of the MoS<sub>2</sub> spiral pyramid. (b) Single edge dislocation (raised blocks, right) and subsequent spiral growth. (c) top down (c-axis) model of 3R-MoS<sub>2</sub> spiral pyramid.

**Figure 10.** Atomic model of spiral WSe<sub>2</sub>. (a) side view and (b) top (c-axis) view. Burgers circuit is represented via red colored atoms, and corresponding burgers vector is represented as a blue arrow.

**Figure 11.** (a) Schematic illustration of screw dislocation driven growth mechanism<sup>[8]</sup>. (b) Schematic illustration of the growth mechanism emphasizing the initial overlapping spiral layers and showing the formation progress of single spiral pattern<sup>[9]</sup>. (c) Schematic illustration of step uplifting mechanism. The terms  $\delta$  and  $\alpha$  represent single layer thickness of a TMD sheet and interlayer spacing between TMD layers, respectively<sup>[10]</sup>. (d) Schematic illustration of the atomic arrangement showing the distinct stacking sequence in spiral TMD. Both layers are in the same direction, and the top layer is translated by a vector  $\mathbf{a}$ . The transition metal atom in the top layer (red hexagon) is positioned at the center of the bottom layer hexagon (blue)<sup>[10]</sup>.

**Figure 12.** Experimental HRTEM image at 80 kV and  $C_s \sim 0 \mu\text{m}$  for monolayer graphene as a function of defocus<sup>[13]</sup>.

**Figure 13.**  $C_s$ - $\Delta f$  table ( $-20 \mu\text{m} \leq C_s \leq 20 \mu\text{m}$ ,  $-10 \text{ nm} \leq \Delta f \leq 10 \text{ nm}$ ) for the simulated HRTEM images of graphene at 80 kV, with  $C_c = 1.41 \text{ mm}$ , and energy distribution extracted from the EELS data<sup>[13]</sup>. The highest dark and bright atom contrasts are obtained for a set of  $C_s$ - $\Delta f$  values marked by the middle diagonals. The two images marked by the red rectangles are in the center of the

highest-contrast diagonal representing optimum contrast values.

**Figure 014.** (a) Schematic representation of STEM imaging modes. (b) atomic resolution HAADF-STEM image showing different types of vacancies and vacancy complexes in MoS<sub>2</sub> monolayers<sup>[14]</sup>.

**Figure 15.** DFTEM images of (a) BN/BN( $\theta=0^\circ$ , parallel), (b) BN/NB( $\theta=60^\circ$ ) stacked h-BN bilayer regions, taken by selecting different diffraction spots in the inset figure ( $\Phi_{o1}$  and  $\Phi_{o2}$  in (a) and  $\Phi_{i1}$  and  $\Phi_{i2}$  in (b))<sup>[16]</sup>. Strain-induced topological defect lines are observed as dark lines as seen in the middle images of (a) and (b). The displacement vectors of topological defects are deduced from their different imaging conditions; defects are invisible at  $\Phi_{o2}$  for BN/BN, while they disappear at  $\Phi_{i2}$  for BN/NB. The lower images are schematics of defect structures under a shear strain, as the displacement vectors  $T$  are in the arm-chair and zig-zag directions for BN/BN and BN/NB, respectively.  $\mathbf{g}_{o2}$  and  $\mathbf{g}_{i2}$  indicate diffraction lattice vectors perpendicular to the diffracting planes for  $\Phi_{o2}$  and  $\Phi_{i2}$ , respectively. For clarity, transitions are exaggerated with respect to the lattice constants. All scale bars are 30 nm.

**Figure 16.** DFTEM images of multilayer WS<sub>2</sub> on graphene obtained from (0-110) and (-2110) diffraction spots of WS<sub>2</sub>, respectively, as indicated by circles in the inset in (b) showing the corresponding diffraction pattern<sup>[17]</sup>. The  $\{-2110\}$  (second order) DFTEM image roughly represents the layer number, as shown in (b). In the bilayer

region, indicated in (b), the layer has different contrast in the  $\{0-110\}$  (first order) DFTEM image, representing AB-AC domains. The scale bars in (a,b) and inset of (b) are 200 and 0.5 nm, respectively.

**Figure 17.** Experimental 4D-STEM measurement of a dichalcogenide 2D material<sup>[21]</sup>. Atomic map is inferred from the data, each diffraction pattern represents an average of  $7 \times 7$  experimental images.

**Figure 18.** Diffraction pattern from a single pixel (top half) and mean of all pixels (bottom half) along with various virtual aperture positions indicated with coloured circles with the corresponding reconstructed images on each corner<sup>[20]</sup>.

**Figure 19.** Schematic illustration of TEM sample preparation, CVD followed by water assisted transfer method<sup>[22]</sup>.

**Figure 20.** (a) HAADF image of WSe<sub>2</sub> spiral. (b) Same HAADF image with an auxiliary line (red) showing that it is spiral. (c) Enlarged image of the blue box in (b). (d) Enlarged image of the red box in (c). (e) Line profile of monolayer region (yellow line). Showing the W atoms and two Se atoms as bright and dim spots respectively. (f) Line profile of bilayer region (Blue line). Intensity of each atomic column is the same which justifies 2H structure.

**Figure 21.** (a) AFM image of WSe<sub>2</sub> spiral showing the height of

each step is monolayer thickness. (b) line profile of red line showing each step height is one layer thick ( $\sim 0.65\text{nm}$ ).

**Figure 22.** (a) HAADF image of spiral  $\text{WSe}_2$  with a colored box for which the line profile is analyzed. (b) HAADF image colored with the color corresponding to the number of layers. Legend is located on the right side. (c) Line profiles in each area colored in (a). (d) Line profile showing the number of layers in each region in the region marked in green in (a). (e) A graph summarizing intensities for each number of layers for each region in (c).

**Figure 23.** (a) HAADF image of  $\text{WSe}_2$  spiral with the number of layer determined. (b–d) Representative diffraction pattern of 4 representative region indicated in (a). Each region corresponds to (b) uniform stacked region, (c) uniform stacked region with carbon grid, (d) Moire region due to the twist of the bottom layer, (e) another Moire region.

**Figure 24.** (a–e) Visualized 4D–STEM data. (a) vADF image, (b) diffraction pattern at the top left corner position of the red box in (a), (c–e) vDF images of the red box area for the three  $\mathbf{g}$  vectors shown in (b). In (d) with  $\mathbf{g}_2$  selected, it can be observed that the contrast disappears in the bilayer region indicated by the red arrow. (f) HAADF image with dislocation information displayed, (g) c–axis direction view of monolayer  $\text{WSe}_2$ . The  $\langle 1-210 \rangle$  direction family and the  $\langle 10-10 \rangle$  direction family are indicated by red arrows. (h)

Acquired selected area electron diffraction pattern of WSe<sub>2</sub> in other microscope (JEM 2100F). The first order diffraction spot  $\{10-10\}$  is expressed in white letters, and the second order diffraction spot  $\{1-210\}$  is expressed in yellow letters. It is an image so that readers can refer to the relationship between each direction.

**Figure 25.** (a) HAADF image of the white boxed area of **Figure 20(c)**, which is the bilayer region. (b) HAADF image of the blue boxed area in **Figure 20(c)**. In the monolayer area where the line defect ends, an intact monolayer is observed without tearing or overlapping. (c) An enlarged image of the red boxed area in (a) showing the position of each atom. Atomic positions with a short period are shown in red, and atomic positions with a long period are shown in yellow. (d) A model in which 26 unit cells (bottom) and 27 unit cells (top) are partially overlapped for the width of  $26a$ , and  $a$  is a unit cell vector. The arrangement of the atomic positions is similar as shown in (c). (e) Image obtained by HAADF simulation of a bilayer structure with 26 unit lattices for the lower layer and 27 unit lattices for the upper layer. The image is similar to (c).

**Figure 26.** Burgers circuit (red arrow), Burgers vector (blue arrow), and dislocation line directions (green arrow) for the proposed model; (a)  $c$ -axis direction view, (b)  $[10-10]$  direction view.

**Figure 27.** (a) HAADF image in bilayer dislocation region. (b) Line profile of the HAADF intensity profile in the red region in (a)

multiplied by  $-1$ . (c) Interplanar interaction energy change graph during the bilayer 2H stacking change process. (d) Graph of strain energy according to strain.

**Figure 28.** (a) HAADF image showing possible stacking sequences. (b) Calculation result of binding energies in 6 possible bilayer stackings. (c) The structure of the 6 possible bilayer stacking.

**Figure 29.** Intensity graph of 6 first order diffraction spots according to each stacking sequence. The inset image displays a representative diffraction pattern and the index of each diffraction spot.

**Figure 30.** Average intensity graph of simulated diffraction patterns according to the stacking sequence. (a) Zone axis condition with no tilt, (b) superimposed graph for each tilt angle,  $\theta$ , shown in legend. effect according to azimuth,  $\phi$ , is expressed as standard deviation at each theta point.

**Figure 31.** Polarity graph of simulated diffraction patterns according to the stacking sequence. (a) Zone axis condition with no tilt, (b) superimposed graph for each tilt angle,  $\theta$ , shown in legend. effect according to azimuth,  $\phi$ , is expressed as standard deviation at each theta point.

**Figure 32.** Reconstructed 4D-STEM image of (a) average intensities and (b) polarity of the first order diffraction peak.



# Chapter 1. Introduction

## 1.1. Van der Waals Materials

Two dimensional (2D) or van der Waals (vdW) material has strong covalent bonds within the single layer, and weak van der Waals bonds between the layers. There are 2D materials such as graphene which is metallic with carbon in a plane, insulating h-BN of boron and nitrogen, and transition metal dichalcogenide (TMD) which can be either semiconducting or metallic with transition metals and chalcogens. **Figure 1** shows some well-known 2D materials<sup>[1]</sup>. Layers in such material have van der Waals force in out-of-plane direction without dangling bonds. For this reason, a layer can be easily exfoliated and transferred, and stacked without lattice mismatch or interface defects<sup>[2]</sup>.

For it can be easily handled layer by layer, distinct layers can be stacked building a heterostructure at the atomic level as shown in **Figure 3**. With this method, devices with new characteristics can be built, combining materials which could not with conventional methods<sup>[1]</sup>.

Graphene family	Graphene	hBN 'white graphene'	BCN	Fluorographene	Graphene oxide
2D chalcogenides	MoS <sub>2</sub> , WS <sub>2</sub> , MoSe <sub>2</sub> , WSe <sub>2</sub>		Semiconducting dichalcogenides: MoTe <sub>2</sub> , WTe <sub>2</sub> , ZrS <sub>2</sub> , ZrSe <sub>2</sub> and so on	Metallic dichalcogenides: NbSe <sub>2</sub> , NbS <sub>2</sub> , TaS <sub>2</sub> , TiS <sub>2</sub> , NiSe <sub>2</sub> and so on	
				Layered semiconductors: GaSe, GaTe, InSe, Bi <sub>2</sub> Se <sub>3</sub> and so on	
2D oxides	Micas, BSCCO	MoO <sub>3</sub> , WO <sub>3</sub>	Perovskite-type: LaNb <sub>2</sub> O <sub>7</sub> , (Ca,Sr) <sub>2</sub> Nb <sub>3</sub> O <sub>10</sub> , Bi <sub>4</sub> Ti <sub>3</sub> O <sub>12</sub> , Ca <sub>2</sub> Ta <sub>2</sub> TiO <sub>10</sub> and so on		Hydroxides: Ni(OH) <sub>2</sub> , Eu(OH) <sub>2</sub> and so on
	Layered Cu oxides	TiO <sub>2</sub> , MnO <sub>2</sub> , V <sub>2</sub> O <sub>5</sub> , TaO <sub>3</sub> , RuO <sub>2</sub> and so on			Others

**Figure 1.** 2D materials library <sup>[1]</sup>. Blue shading indicates monolayers that have been proved to be stable at room temperature in air. Green shading indicates monolayers that are probably stable in air. Pink shading indicates monolayers that are unstable in air but may be stable in inert atmosphere. Grey shading indicates 3D compounds that have been successfully exfoliated down to monolayers.

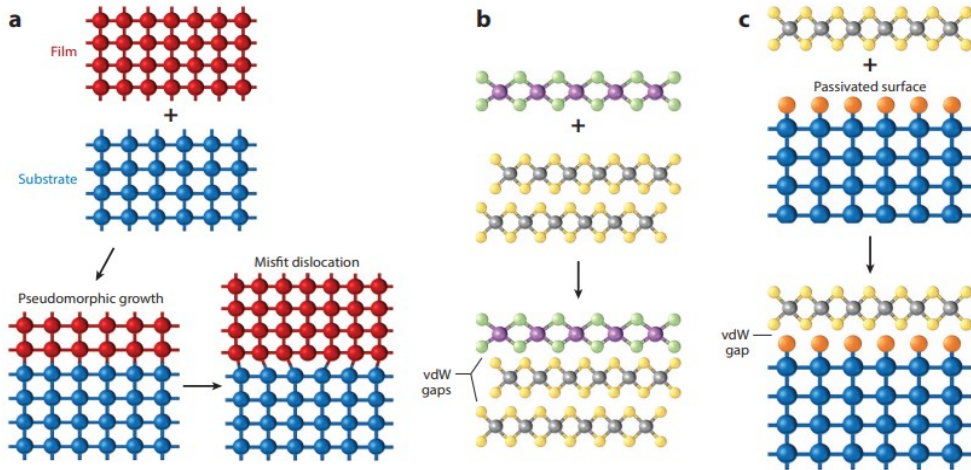


**Figure 2.** Schematic illustrations of (a) conventional epitaxy in which misfit dislocations nucleate to mitigate the stress due to lattice mismatch, (b) van der Waals epitaxy in which both the films and the substrate have no dangling bonds, and (c) vdW epitaxy on a passivated conventional 3D substrate <sup>[2]</sup>.

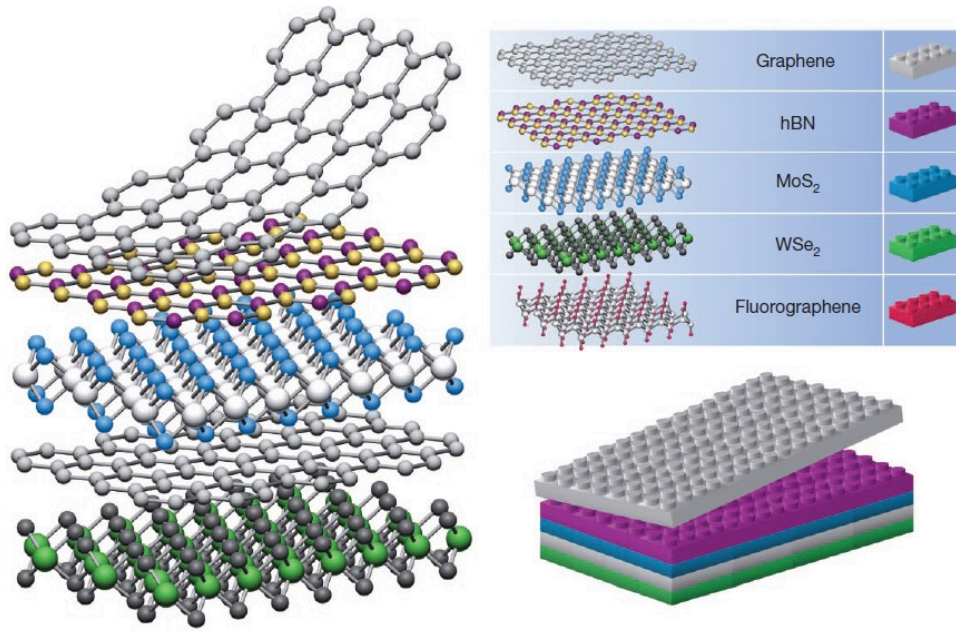


**Figure 3.** Schematic illustration of building van der Waals heterostructures as building Lego blocks<sup>[1]</sup>. Conceptually, this atomic-scale Lego resembles molecular beam epitaxy but employs different construction rules and a distinct set of materials.

TMD is a material group consisting of transition metal and chalcogen. There are generally well-known Mo series and W series, but other materials have not been researched as they are metallic, or unstable in air for semiconductor devices.

In this study, the structure of pyramid-shaped spiral TMD generated when TMD materials are grown by chemical vapor deposition (CVD) was analyzed. **Figure 4** shows a schematic diagram and an atomic force microscope (AFM) image of the spiral growth of MoS<sub>2</sub><sup>[4]</sup>. It has investigated that the spiral structure is from screw dislocation driven growth (SDD growth), in which a

screw dislocation is formed in the center, by confirming the image of continuous spirally grown structure and that the thickness of each spiral edge is one layer thick through AFM analysis<sup>[3]</sup>.

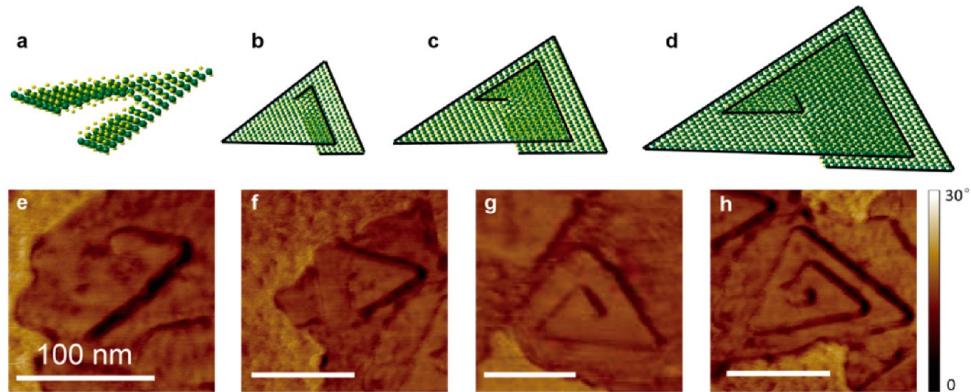


**Figure 4.** Growing mechanism of atomic layered MoS<sub>2</sub> spiral<sup>[4]</sup>. (a–d) Schematic illustration of MoS<sub>2</sub> spiral from nucleation to growth. Black lines indicate the exposed edges. (e–h) AFM images (phase signal) of several typical spirals at different growth stages. The growth will start from (e) a slipped edge and generate (f) a small spiraled triangle. With growth continued, the generated dislocation core will keep spiraling up vertically and form (g,h) pyramid-shaped 3D large spirals.

**Figure 5** shows the scanning electron microscope (SEM) image of the MoS<sub>2</sub> spiral and the cross-sectional transmission electron microscope (TEM) image of the area including the screw dislocation. **Figure 5(a)** shows a MoS<sub>2</sub> pyramid coated with a layer of carbon and platinum to protect it before sectioning. An intercalated stacking of MoS<sub>2</sub> originated by the screw dislocation closer to the center of the pyramid is observed in **Figure 4(b)**.

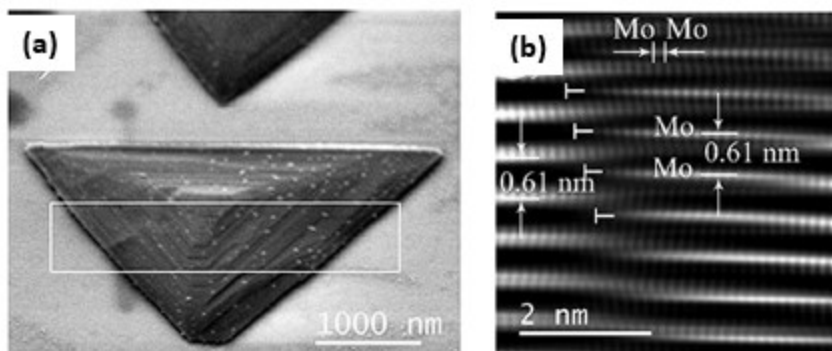


**Figure 5.** (a) SEM image of the MoS<sub>2</sub> pyramid with a white rectangle where the cross-section cut was made. (b) Atomic resolution imaging of the layer stacking of MoS<sub>2</sub>.

Previous studies have analyzed the structure of spiral TMDs using AFM, TEM, and optical analysis. However, it has not been studied enough on the stacking order of each layer of the spiral TMD and the Burgers vector of the central threading dislocation.

Spiral TMDs can be utilized in various ways according to their structural characteristics. In the case of a conductive TMD material, the electrical conductivity is excellent in the in-plane direction, but lower in a few orders between the planes because there are almost no electrical interactions but only van der Waals interactions.

As shown in **Figure 6(a)**, the current flows spirally along the plane when a vertical electric field is applied in the spiral structure<sup>[5]</sup>. Also, the spiral pyramid structure has a high density of edge sites on the exposed surface. As shown in **Figure 6(b)**, the edge site becomes an active site for the electrocatalytic reaction, and the spiral TMD can be used as efficient electrodes for the electrocatalytic reaction<sup>[6]</sup>.

The characteristics of the device may deteriorate if the spiral TMD has any defects. However, the defects in spiral TMDs are not studied sufficiently.

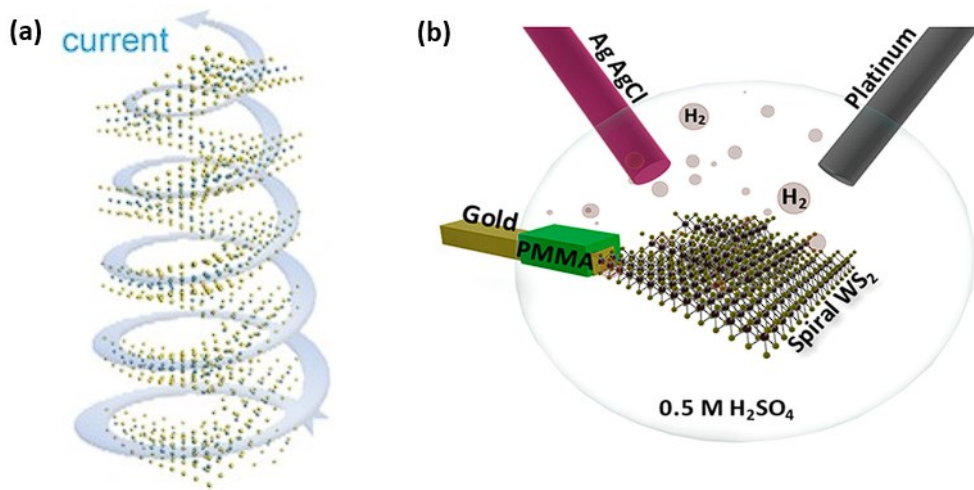


**Figure 6.** Application of spiral TMD. (a) Schematic illustration of helical current of spiral MoS<sub>2</sub><sup>[5]</sup>. (b) Schematic illustration of electrochemical microcell assembly. WS<sub>2</sub> with many active sites is used as an electrode for hydrogen generation reaction<sup>[6]</sup>.

## 1.2. Structure of spiral TMD

Monolayer TMD has a hexagonal unit cell. In **Figure 7(c, d)**, the three sites in a unit cell in which W, Se, or vacancy can be located are marked as A, B, and C. **Figure 8** shows two possible WSe<sub>2</sub> monolayer structures. These two monolayers cannot be overlapped by translation, but only by rotation of 60 or 180 degrees. These two monolayers are said to be antiparallel to each other.

**Figure 7** summarizes the two most stable structures of TMD, stacked parallel or antiparallel. The most stable structure in antiparallel stackings is shown in **Figure 7(a, c)**. The two adjacent layers have the transition metal and chalcogen sites reversed, but the same vacancy at the C site. This is called a 2H structure which has the hexagonal unit cell composed of two antiparallel layers. It is also called AA' stacking as the antiparallel A' layer is stacked on the A layer.

In the other hand, the most stable structure in parallel stackings is shown in **Figure 7(b, d)**. This structure consists of all parallel planes, and the displacement of adjacent layers is constant. **Figure 7(b)** shows the positions of the chalcogen elements, from the bottom layer to the top layer, are translated step by step in order of A-C-B-A-..., respectively. This is called a 3R structure which has the rhombohedral unit cell composed of three parallel layers. It is also called ABC stacking as the three layers has different displacement layer by layer. At room temperature, the 2H structure is slightly more stable than the 3R structure, but since the transition

from the 3R structure to the 2H structure requires surface rotation, which does not occur below 500°C<sup>[7]</sup>.

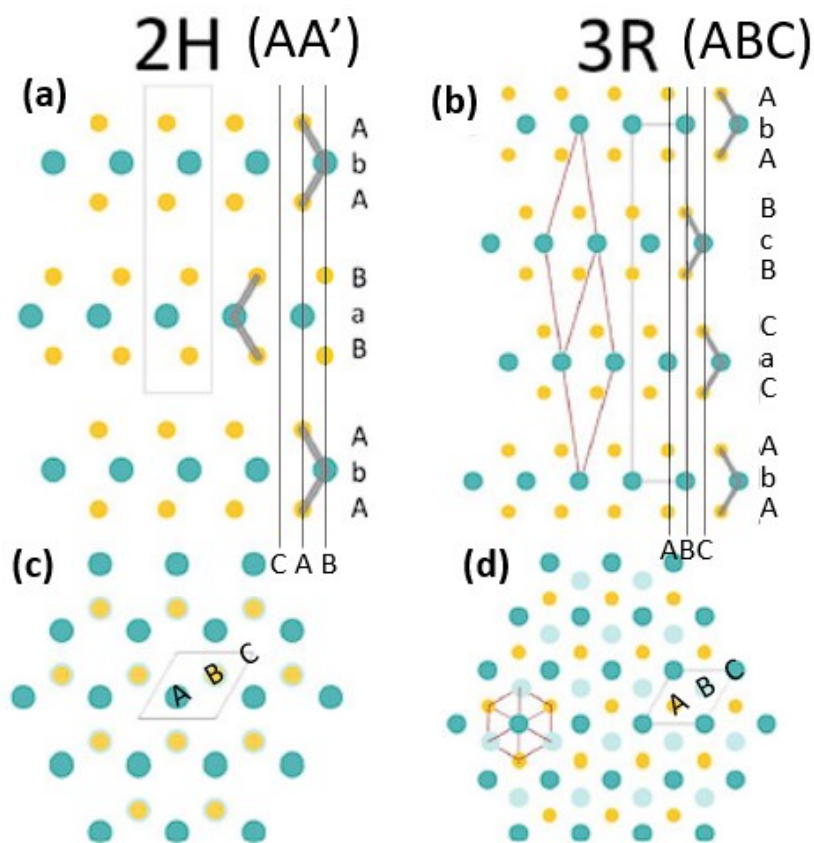


**Figure 7.** Crystal structures of the most common TMD polytypes: 2H(a, c; ICSD, 24000) and 3R(b, e; ICSD, 38401)<sup>[7]</sup>. (a, b) Crystals viewed along the a-axis, where the unit cell is shown as a grey box and 3R rhombohedral unit cell is shown as a red box. Layer directions shown by grey chevrons and layer names on the right. (c, d) Bilayers viewed along the c-axis.



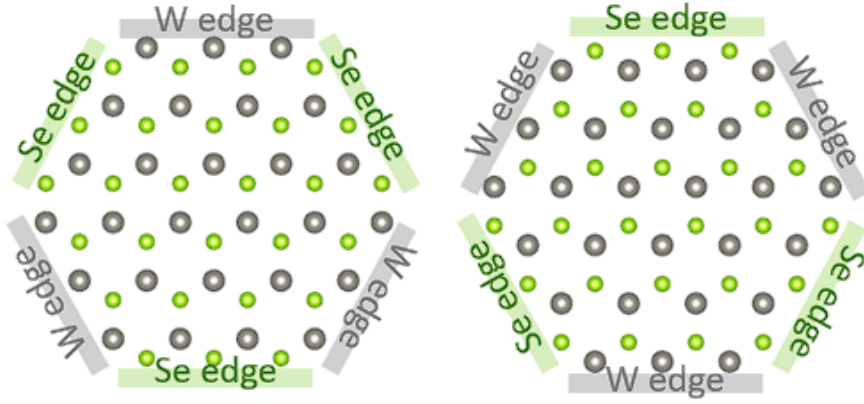


**Figure 8.** Two WSe<sub>2</sub> monolayer which is antiparallel. The atoms on the edge sites are indicated. Each layer can be overlapped to the other when the layer is rotated by 60° or 180°.

Here, the spiral TMD is believed to follow the screw dislocation driven (SDD) growth model, which is the most favorable mode of growth at low supersaturation<sup>[8,11]</sup>. **Figure 9** is a schematic diagram of the growth model. From this model, in case of spiral growth, one layer in the vertical direction steps up for each revolution in horizontal direction, as **Figure 10** shows in detail. In other words, when drawing a Burgers circuit, the Burgers vector has a size equal to the thickness of the monolayer in the *c* direction. The Burgers circuit and the Burgers vector are indicated by red arrows and a blue arrow, respectively. And the line defect forming the Burgers vector is screw dislocation parallel to the Burgers vector. This screw dislocation is indicated by a green arrow.

According to previous studies, 2H stacking cannot occur in spiral TMDs because the monolayer grows continuously<sup>[4]</sup>. During continuous growth, the planes must remain parallel, but in order to

grow into a 2H structure, the direction must change antiparallel as it spirals up. Instead, each layer of the spiral TMD grows in parallel, like a 3R structure <sup>[7]</sup>.

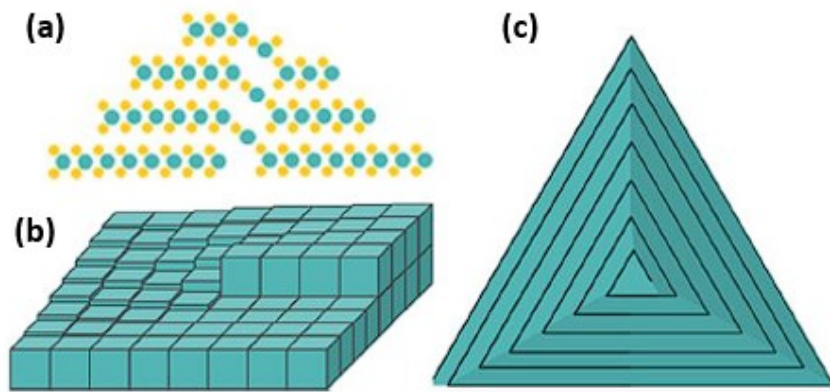


**Figure 9.** Screw dislocation growth diagrams<sup>[7]</sup>. (a) side on (a-axis) model of the MoS<sub>2</sub> spiral pyramid. (b) Single edge dislocation (raised blocks, right) and subsequent spiral growth. (c) top down (c-axis) model of 3R-MoS<sub>2</sub> spiral pyramid.

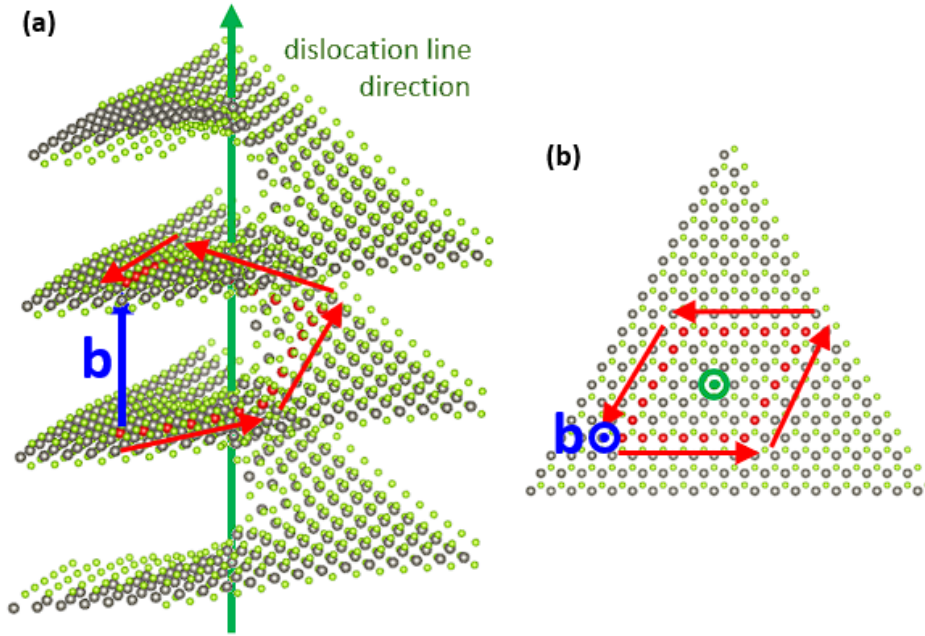


**Figure 10.** Atomic model of spiral WSe<sub>2</sub>. (a) side view and (b) top (c-axis) view. Burgers circuit is represented via red colored atoms, and corresponding burgers vector is represented as a blue arrow.

The spiral TMD growth mechanism presented in previous studies is summarized in **Figure 11**. As shown in **Figure 11 (a, b)**, one layer accidentally climbs on top of another layer due to substrate irregularities or growth under supersaturated conditions. After that, the edge which has faster growth rate becomes sharp, forms a triangular spiral pyramid, and grows gradually<sup>[8]</sup>. As a layer is covered by another, the covered edge cannot be supplied any material and stops growing, while the edges exposed to the outside still grow. The shape of the covered edge of the bottom layer that cannot grow is shown step by step in **Figure 11(b)**<sup>[9]</sup>. Each edge of the triangular facet, consequently, has the lower growth rate. The

width of the terrace between steps is determined according to the ratio of the upward growth rate ( $R_m$ ) and the horizontal growth rate ( $v_s$ ) of the edge, which is shown in **Figure 11(a)**.

**Figure 11(c)** shows how the screw dislocation creates. When two TMD domains intersect (step 1), it can cause an uplifting of one grain boundary (step 2). The uneven surface of the substrate which is caused by the partial etching of  $\text{SiO}_2/\text{Si}$  with piranha and plasma treatment also catalyzes the spiral growth<sup>[10]</sup>. This process will leave some unsaturated chalcogen atoms hanging on this uplifted edge forming a second layer growth. Once the second layer is extended, a screw dislocation will be created, which facilitates further spiral growth of TMD following SDD model (step03)<sup>[8]</sup>. As a result, two layers are parallel and the top layer is translated by a vector  $\mathbf{a}$  in **Figure 11(d)**. However, the specific direction and size of translation vector has not been clearly identified yet.

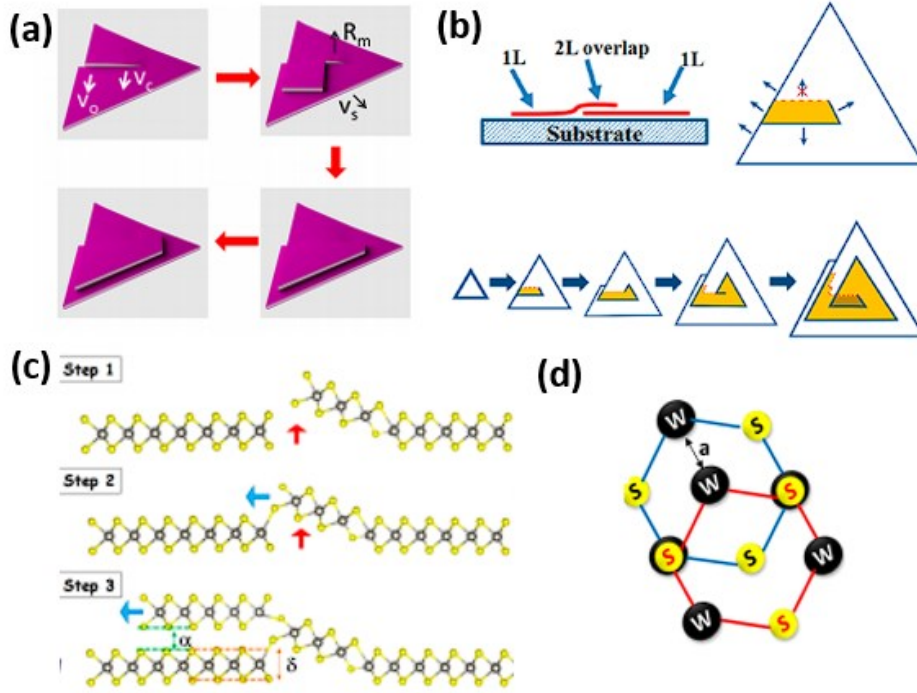


**Figure 11.** (a) Schematic illustration of screw dislocation driven growth mechanism<sup>[8]</sup>. (b) Schematic illustration of the growth mechanism emphasizing the initial overlapping spiral layers and showing the formation progress of single spiral pattern<sup>[9]</sup>. (c) Schematic illustration of step uplifting mechanism. The terms  $\delta$  and  $\alpha$  represent single layer thickness of a TMD sheet and interlayer spacing between TMD layers, respectively<sup>[10]</sup>. (d) Schematic illustration of the atomic arrangement showing the distinct stacking sequence in spiral TMD. Both layers are in the same direction, and the top layer is translated by a vector  $\mathbf{a}$ . The transition metal atom in the top layer (red hexagon) is positioned at the center of the bottom layer hexagon (blue)<sup>[10]</sup>.

### 1.3. Transmission electron microscopy analysis

TEM is a powerful analytical instrument that can observe the crystal structure of materials on a sub-nanometer scale. The latest aberration corrected TEM of which resolution raised to the limit can perform picometer-level analysis<sup>[12]</sup>. Therefore, TEM analysis is essential to analyze the exact structure of TMD materials. TEM analysis is largely divided into parallel beam illumination and convergent beam illumination.

#### 1.3.1 High resolution transmission electron microscopy (HRTEM)

HRTEM imaging, which is also called a phase contrast imaging, is a technique that obtains a projected image by irradiating a collimated beam. It measures the wavefunction of electrons interacting with the sample.

However, in the case of HRTEM imaging technique, it is difficult to associate bright and dark patterns with atomic columns, since the contrast of fine features of a material change according to the objective lens aberration, such as defocus or spherical aberration<sup>[13]</sup>. **Figure 12** shows how the HRTEM image of monolayer graphene changes after defocus. The carbon atoms of graphene are presented as dark dots sometimes, or bright dots at the other. **Figure 13** is a simulated image table by changing defocus and spherical aberration, which implies the same result. In other words, direct interpretation of an HRTEM image is difficult because the contrast changes according to the aberration.

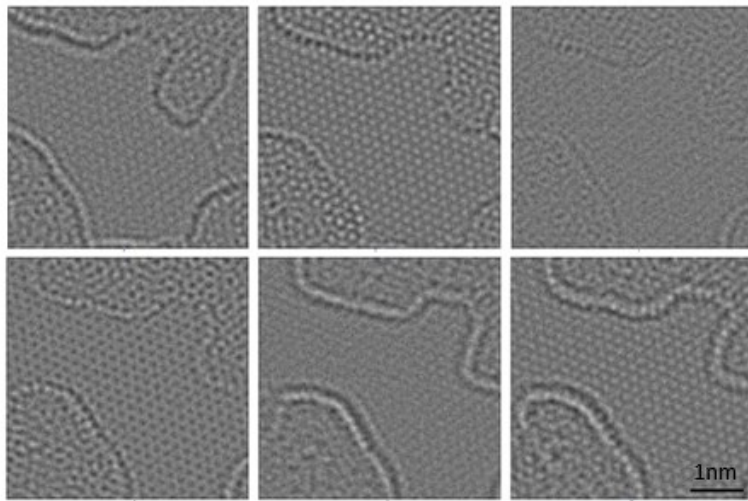
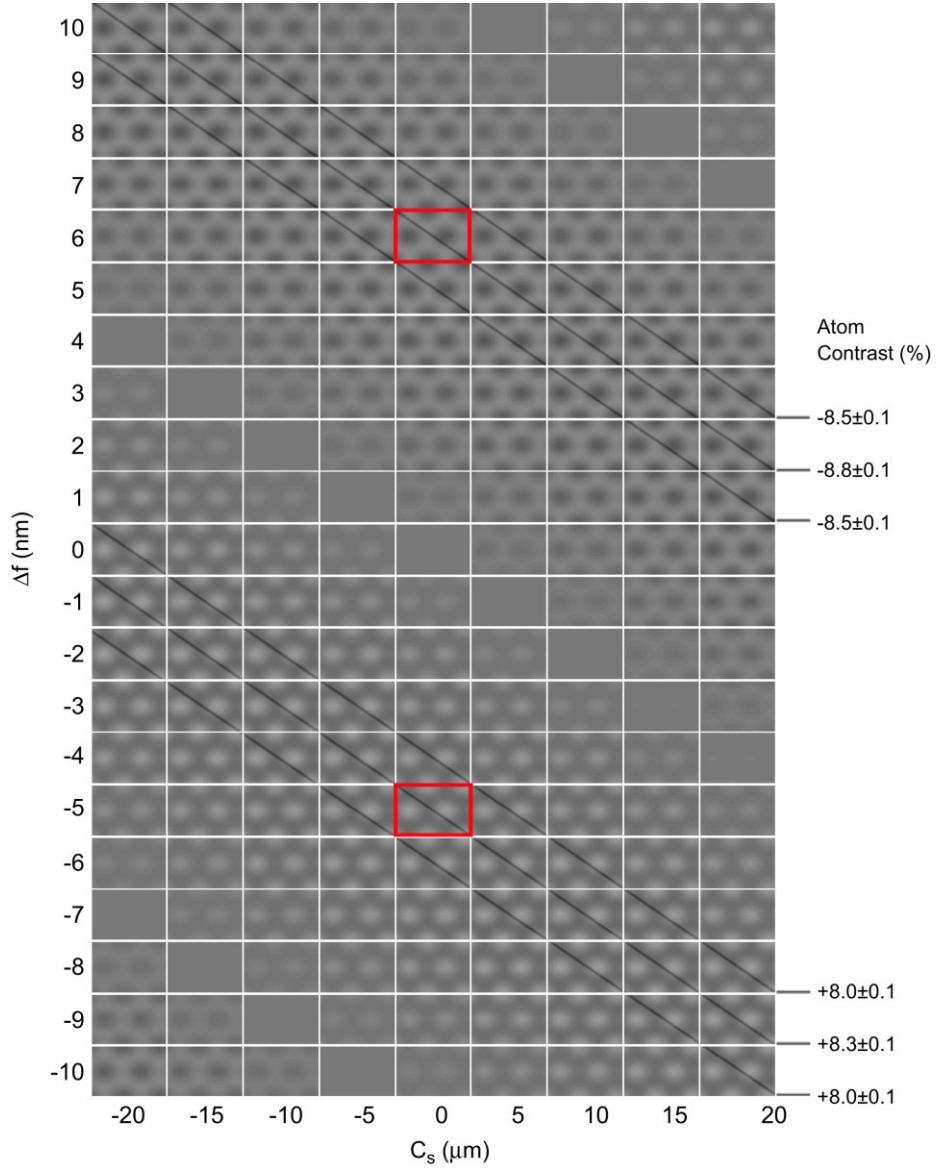


**Figure 12.** Experimental HRTEM image at 80 kV and  $C_s \sim 0 \mu\text{m}$  for monolayer graphene as a function of defocus<sup>[13]</sup>.





### 1.3.2. High angle annular dark field scanning transmission electron microscopy (HAADF STEM)

One of the most representative imaging technique using a convergent beam is HAADF imaging. **Figure 14(a)** is a schematic diagram of HAADF imaging.  $C_s$ -corrected STEM scans a sample with a very fine electron probe below 100 pm<sup>[14]</sup>. The HAADF image cancels the coherency of the electron beam by summing both elastic and inelastic scattered electrons at high angles<sup>[15]</sup>. As a result, the HAADF image shows incoherent Z contrast. In the HAADF image, the greater the atomic number Z and the thicker the sample, the greater the intensity. Accordingly, as shown in **Figure 14(b)**, it is possible to be interpreted directly that the region with higher intensity has the thicker, and the higher atomic number of which atomic column is located.

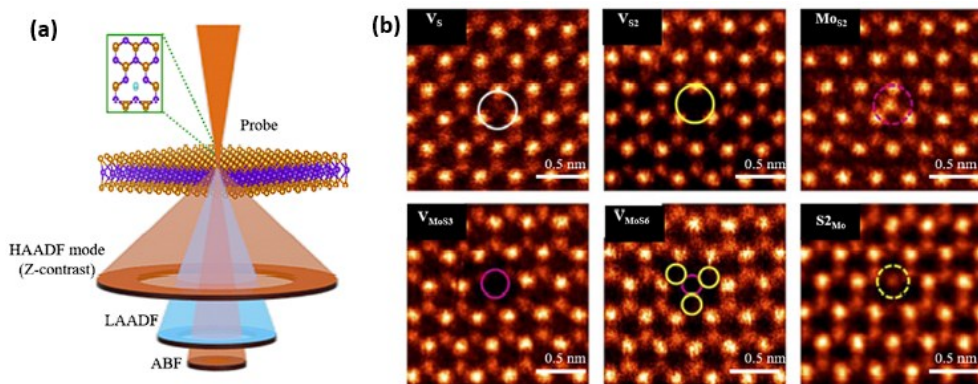


**Figure 014.** (a) Schematic representation of STEM imaging modes. (b) atomic resolution HAADF-STEM image showing different types of vacancies and vacancy complexes in MoS<sub>2</sub> monolayers<sup>[14]</sup>.

### 1.3.3. Dark field transmission electron microscopy (DFTEM)

DFTEM imaging is a powerful tool to analyze the stacking of two-dimensional materials. According to previous studies, DFTEM was used to confirm the stacking of h-BN or TMD-shaped materials and analyze line defects<sup>[16, 17]</sup>. DFTEM selects and images only electrons diffracted in a specific direction, the  $\mathbf{g}$  direction, from the diffraction pattern of the specimen. A bright area in a DFTEM image indicates that electrons are diffracted in the selected  $\mathbf{g}$  direction.

**Figure 15** shows DFTEM images obtained with different diffraction peaks. As the DFTEM image considers diffraction in the selected  $\mathbf{g}$  direction only, any structural characteristic that has no  $\mathbf{g}$  directional component does not make contrast on the image<sup>[18]</sup>. In other words, there is no contrast if the dot product of the displacement vector,  $\mathbf{T}$  and  $\mathbf{g}$  vector is 0. With this feature, the direction of the Burgers vector or displacement vector of a dislocation can be obtained.

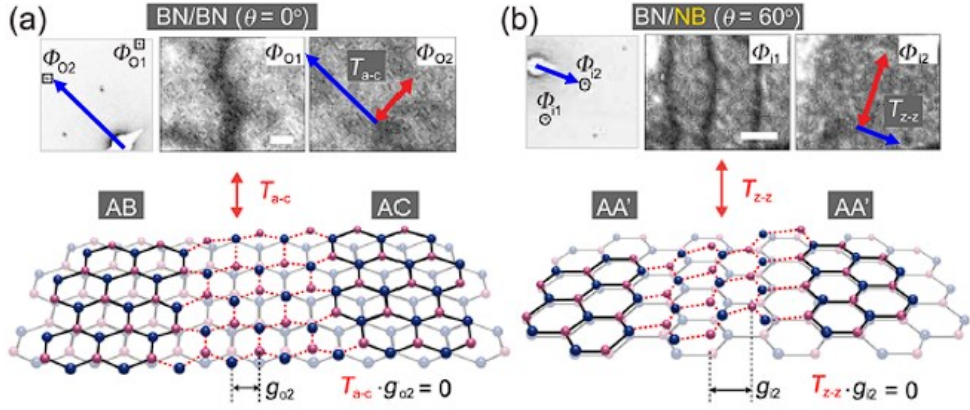


**Figure 15.** DFTEM images of (a) BN/BN( $\theta=0^\circ$ , parallel), (b) BN/NB( $\theta=60^\circ$ ) stacked h-BN bilayer regions, taken by selecting different diffraction spots in the inset figure ( $\Phi_{01}$  and  $\Phi_{02}$  in (a) and  $\Phi_{i1}$  and  $\Phi_{i2}$  in (b))<sup>[16]</sup>. Strain-induced topological defect lines are observed as dark lines as seen in the middle images of (a) and (b). The displacement vectors of topological defects are deduced from their different imaging conditions; defects are invisible at  $\Phi_{02}$  for BN/BN, while they disappear at  $\Phi_{i2}$  for BN/NB. The lower images are schematics of defect structures under a shear strain, as the displacement vectors  $T$  are in the arm-chair and zig-zag directions for BN/BN and BN/NB, respectively.  $\mathbf{g}_{02}$  and  $\mathbf{g}_2$  indicate diffraction lattice vectors perpendicular to the diffracting planes for  $\Phi_{02}$  and  $\Phi_{i2}$ , respectively. For clarity, transitions are exaggerated with respect to the lattice constants. All scale bars are 30 nm.

In HAADF-STEM image, it is difficult to distinguish between AB and AC stackings. However, as shown in **Figure 16(a)**, AB and AC stackings make different diffraction patterns, so the intensities in the DFTEM image become different<sup>[17]</sup>. In detail, in the inset image of **Figure 16(b)**, the innermost blue ring includes  $\{0-110\}$  plane family or first order diffraction spots. And the gray ring includes  $\{-2110\}$  plane family or second diffraction spots. In bilayer region in **Figure 16**, DFTEM image using the first order spot shows different intensity for AB, and AC stacked domains. DFTEM image using the second order spot shows that the more the number of layers are, the stronger the intensity is.

From this point of view, stacking sequence of the layers in spiral TMD can be inferred by matching the measured diffraction pattern of the region of interest with the simulated diffraction patterns.

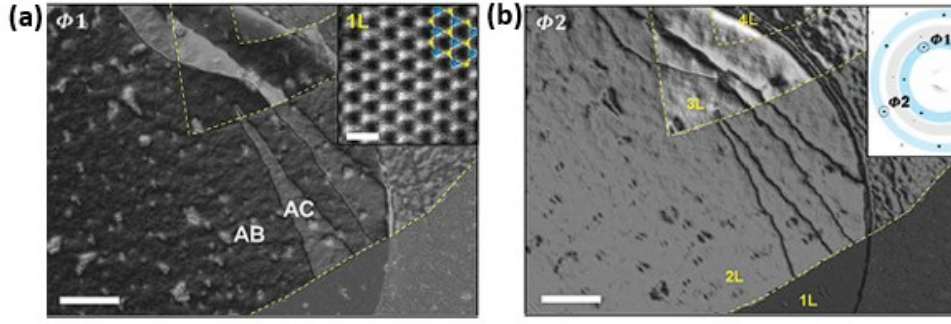


**Figure 16.** DFTEM images of multilayer  $\text{WS}_2$  on graphene obtained from  $(0-110)$  and  $(-2110)$  diffraction spots of  $\text{WS}_2$ , respectively, as indicated by circles in the inset in (b) showing the corresponding diffraction pattern<sup>[17]</sup>. The  $\{-2110\}$  (second order) DFTEM image roughly represents the layer number, as shown in (b). In the bilayer region, indicated in (b), the layer has different contrast in the  $\{0-110\}$  (first order) DFTEM image, representing AB-AC domains. The scale bars in (a,b) and inset of (b) are 200 and 0.5 nm, respectively.

#### 1.3.4. 4 dimensional-scanning transmission electron microscopy (4D-STEM)

With images from collimated beam, there is physical size limit of the selected area aperture, so that it is difficult to observe diffraction characteristics in an area smaller than  $1\ \mu\text{m}$ <sup>[19]</sup>. For such a small area, the nanobeam electron diffraction technique is used. Nanobeam diffraction is a technique to obtain a diffraction pattern in a very small local area of 1 nm by shooting a nearly parallel electron beam at a convergence angle within 1 mrad using a TEM lens and an aperture<sup>[20]</sup>.

**Figure 17** is a schematic diagram showing the measurement process of 4D-STEM<sup>[21]</sup>. A 2D diffraction pattern in a small local area can be obtained by conducting nanobeam diffraction, and this local diffraction pattern is saved for every scanning point in the 2D real space. The 4D data is obtained as a result.

**Figure 18** shows various methods of visualizing the obtained 4D data as a 2D image. First of all, in the middle of the picture, there are a single diffraction pattern of each scanning position and an averaged diffraction pattern of selected scanning positions. It is possible to perform virtual aperture imaging, in which electrons diffract into a specific area can be selected. **Figure 18** shows 4 different images from a 4D-STEM data: a virtual bright field (vBF) image which collects the center beams at the top-left corner, a virtual annular dark field (vADF) image from the ring right adjacent to the center disk at the bottom-left, a virtual dark field (vDF) image from the diffraction peaks in the specific direction at the top-right, and a virtual dark field (vDF) image from the regions deviating from the main diffraction pattern at the bottom-right.

Conventional objective lens apertures were circular, but since the virtual aperture can be selected as desired in pixel units in a diffraction pattern, imaging can be performed by integrating atypical apertures or plane families at once. In addition, since various virtual aperture images can be obtained with a single acquisition, various features can be analyzed at the same time.

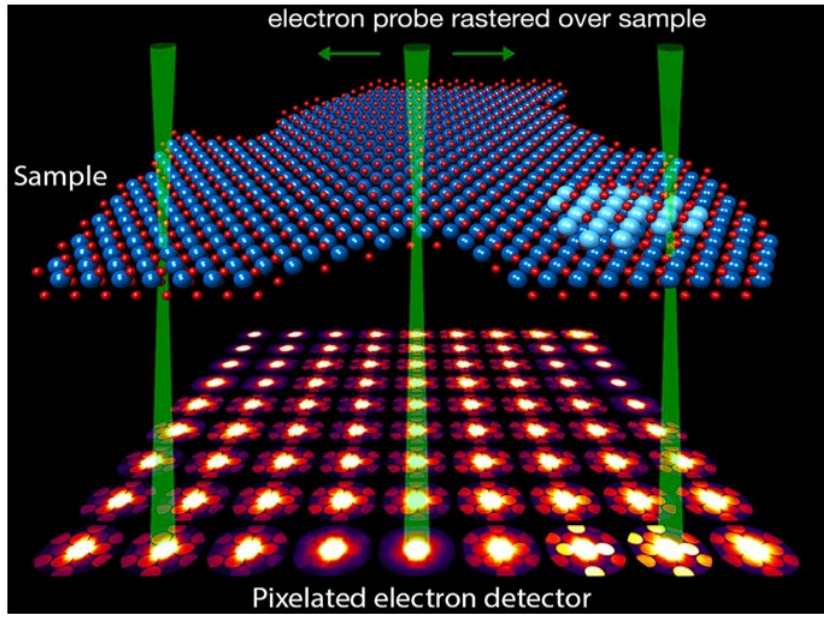


**Figure 17.** Experimental 4D-STEM measurement of a dichalcogenide 2D material<sup>[21]</sup>. Atomic map is inferred from the data, each diffraction pattern represents an average of  $7 \times 7$  experimental images.

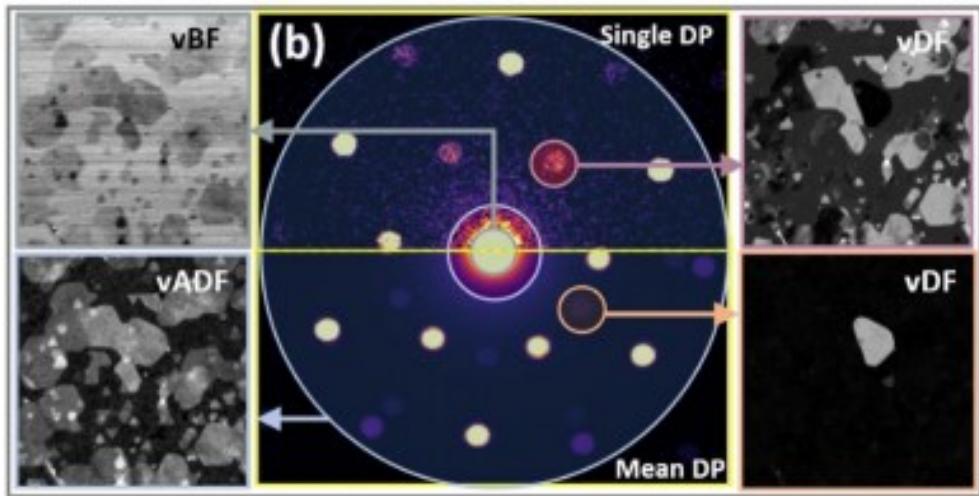


**Figure 18.** Diffraction pattern from a single pixel (top half) and mean of all pixels (bottom half) along with various virtual aperture positions indicated with coloured circles with the corresponding reconstructed images on each corner<sup>[20]</sup>.

## Chapter 2. Experimental Methods

### 2.1. Synthesis of spiral WSe<sub>2</sub>

B<sub>2</sub>O<sub>3</sub> assisted synthesis of WSe<sub>2</sub> was conducted in atmospheric pressure with conventional chemical vapor deposition (CVD) method. An alumina boat with 90 mg of WO<sub>2.9</sub> and 5 mg of B<sub>2</sub>O<sub>3</sub> was placed at the center of furnace. Silicon wafer with 285 nm SiO<sub>2</sub> was placed upside down on mixed powder. A quartz boat with 3 selenium shot was placed 20 cm away from center of furnace. Reaction temperature was 850°C and total reaction time is 15 minute with ramping temperature of 50°C/min, 300 sccm of Ar and 20 sccm of H<sub>2</sub> was introduced to tube during reaction.

### 2.2. Specimen preparation and TEM analysis

The TEM specimen is prepared by transferring the material via water-assisted transfer method on holey carbon supports on 200 mesh Au grid. Schematic illustration of the preparation process is shown in **Figure 19**.



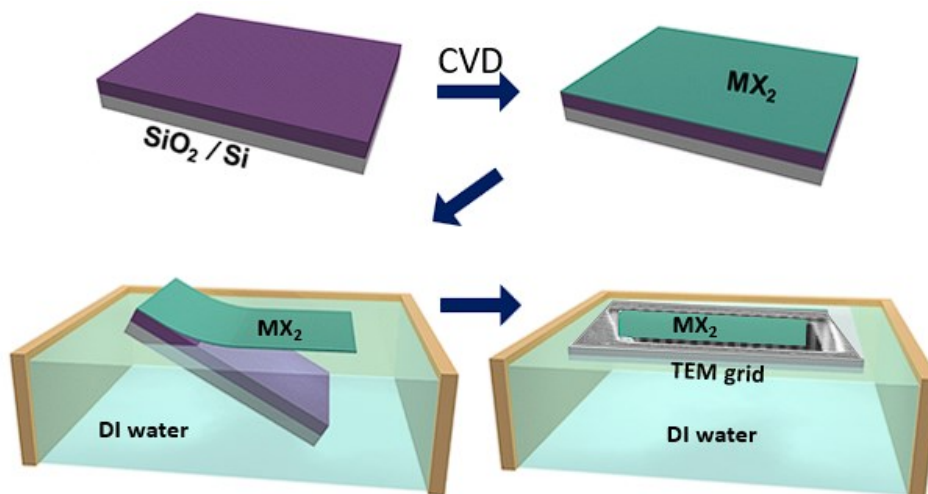


**Figure 19.** Schematic illustration of TEM sample preparation, CVD followed by water assisted transfer method<sup>[22]</sup>.

## 2.3. TEM analysis

TEM measurements were performed on Cs-corrected TEM, (Themis Z, Thermo Fisher) at Research Institute of Advanced Material, Seoul National University. All measurements were operated at an accelerating voltage of 80 kV. Before the measurement, the empty TEM holder is cleaned for 5 minutes using plasma cleaner. And the TEM sample grid is illuminated by the halogen lamp for 1 hour in a transparent vacuum chamber.

HAADF-STEM measurements were carried out to image the position of atoms and to determine the thickness of the region of interest. HAADF-STEM images are acquired with a convergence angle of 23.0 mrad and STEM detector collection angle from 32 to 196 mrad.

4D-STEM measurements were performed to determine the stacking sequence of the spiral WSe<sub>2</sub> sample. The nanobeam electron diffraction pattern was collected at each pixel on the specimen, using an electron microscopy pixelated array detector (EMPAD, 128\*128 pixels). 4D-STEM measurements were obtained at a convergence angle of 2.0 mrad.

Atomic force microscopic measurements were carried out using NX-10 (park systems) at Research Institute of Advanced Material, Seoul National University to image and measure the step height.

## 2.4. Electron diffraction simulation

Electron diffraction simulations to calculate diffraction peak intensities of monolayer, and multilayer WSe<sub>2</sub> are carried out using muSTEM simulation package<sup>[23]</sup>. The accelerating voltage is 80 kV, probe convergence semi-angle is 2.0 mrad. Specimen is tilted to various angle in spherical coordinate. The simulated tilt angles are  $\theta$  from 0 to 100 mrad at 5 mrad intervals,  $\phi$  (azimuth) from 0 to  $\pi/2$  rad with  $\pi/20$  rad intervals.

## 2.5. Computational details

The density functional theory (DFT) calculations were performed by the Vienna ab initio simulation package (VASP). The projector augmented wave (PAW) method was applied for the interactions between the valence electrons and the ionic cores. Generalized gradient approximation (GGA) in the formulation of

Perdew–Burke–Emzerhof (PBE) was employed for exchange–correlation functional. The electron wave function was expanded in a basis set of plane waves with a kinetic energy cut off of 500 eV. The atomic positions of the bilayer WSe<sub>2</sub> with 6 atoms with vacuum layer of 15 Å were fully relaxed until that all forces were smaller than 0.01 eV/Å, with a 10x10x10 gamma centered k–point set. The convergence threshold for self–consistent field (SCF) iteration was set at 10<sup>−7</sup> eV. Spin–polarized calculations were conducted for all models. Van der waals interactions were considered to predict plausible interlayer distance between the layers.

## Chapter 3. Results and Discussion

In the previous chapter, it was mentioned that the analysis of defects in the spiral TMD was not well established, and studies for specific stacking was insufficient. In this chapter, we analyze the line defects that occur in spiral TMD in detail and present a technique to analyze stacking sequence.

### 3.1. Analysis of edge dislocation in bilayer WSe<sub>2</sub>

In this section, we take a closer look at the structure of the spiral TMD, which is layered in a helical fashion. The number of layers in each visible domain is analyzed, and an edge dislocation in the bilayer region is observed and analyzed at the atomic level.

#### 3.1.1. Determination of the number of WSe<sub>2</sub> layers

A HAADF image of a spiral TMD is shown in Figure 020. To help confirm that it is a spiral, it is marked with a red line in **Figure 20(b)**. When drawing along the edge from the outer boundary, it can be seen that one plane has grown continuously in a spiral fashion. AFM measurements were performed to confirm that each edge corresponds to one layer, and the results are shown in **Figure 21**. It is confirmed that the step height of each edge is equal to the thickness of one layer with an average value of 0.65 nm<sup>[3]</sup>.

This means that the spiral TMD has a screw dislocation with a Burgers vector of one layer thickness. According to the elastic theory, if the step becomes bilayer, the strain energy applied to the screw dislocation core is quadrupled, and if the step becomes trilayer, the strain energy is nine folded. Accordingly, it has been reported that the possibility of multilayer screw dislocations is low<sup>[24]</sup>.

**Figure 20(d)** is an enlarged image of the red box area in **Figure 20(c)**. The typical intensity distribution of the monolayer TMD can be seen in the lower right area. A bright tungsten atom and dark selenium atoms alternately show a honeycomb structure, it is confirmed that the corresponding region is a monolayer region. The line profile of the intensity in the area marked in yellow in **Figure 20(d)** is shown in **Figure 20(e)**. In addition, the upper left region can be expected to have a bilayer 2H structure based on the fact that all atomic columns have the same brightness. The line profile of the intensity in the area marked in blue in **Figure 20(d)** is shown in **Figure 20(f)**.

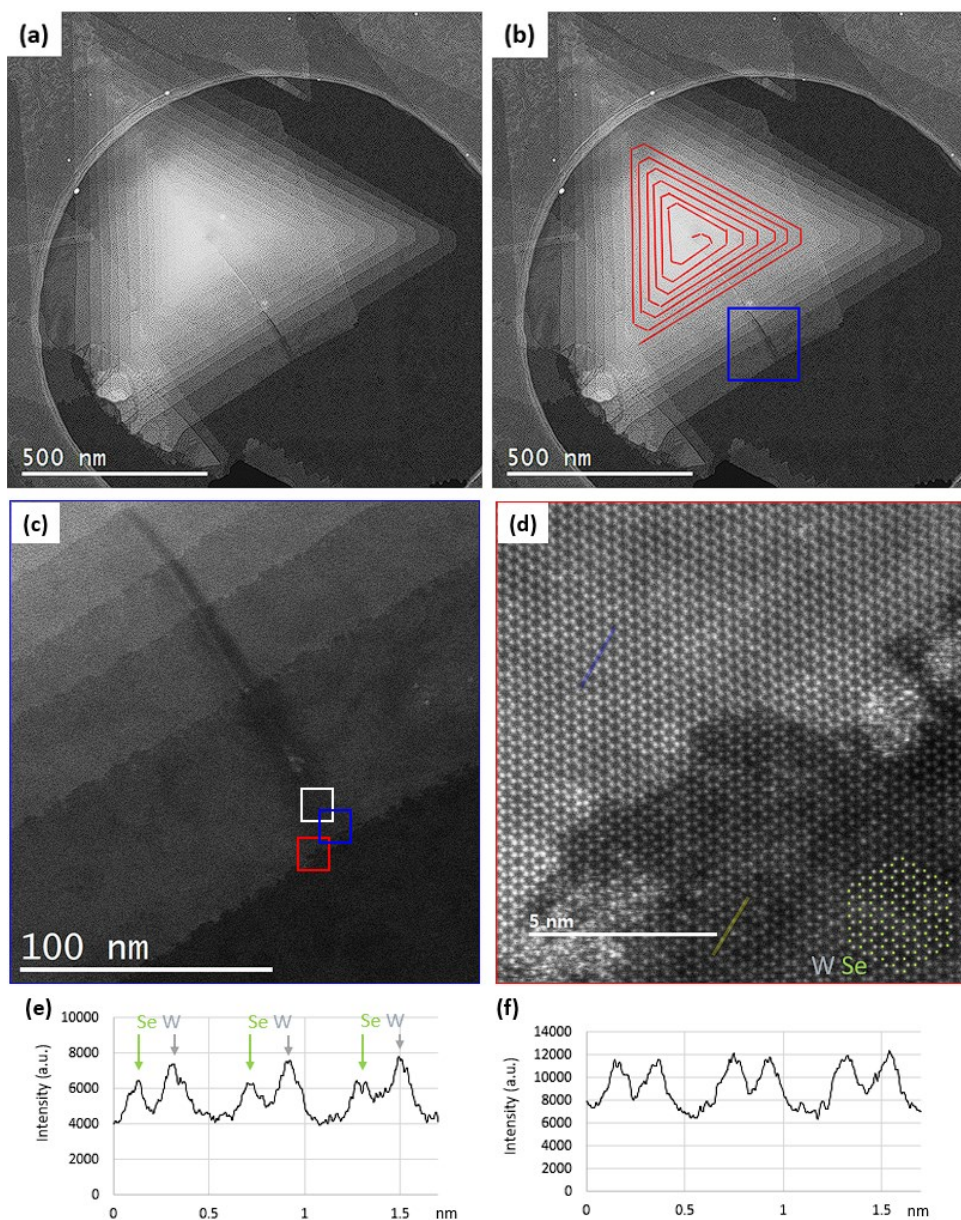


**Figure 20.** (a) HAADF image of WSe<sub>2</sub> spiral. (b) Same HAADF image with an auxiliary line (red) showing that it is spiral. (c) Enlarged image of the blue box in (b). (d) Enlarged image of the red box in (c). (e) Line profile of monolayer region (yellow line). Showing the W atoms and two Se atoms as bright and dim spots respectively. (f) Line profile of bilayer region (Blue line). Intensity of each atomic column is the same which justifies 2H structure.

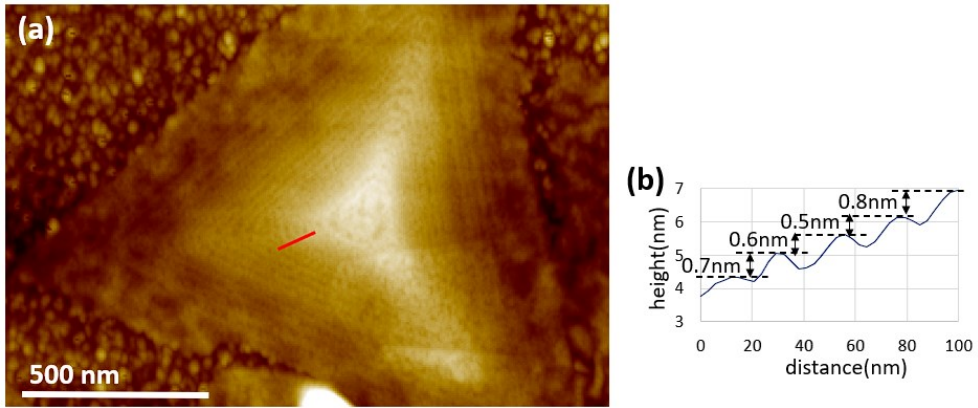


**Figure 21.** (a) AFM image of WSe<sub>2</sub> spiral showing the height of each step is monolayer thickness. (b) line profile of red line showing each step height is one layer thick ( $\sim 0.65$ nm).

The line profile of the HAADF intensity in the area marked with the color box in **Figure 22(a)** is shown in **Figure 22(c)**. Uniform intensity is shown in areas with the same number of layers, and discontinuous jumps in intensity can be seen when going to areas with different numbers of layers.

The graph in **Figure 22(d)** is the line profile in the green area at the top in **Figure 22(a)**. Since it was confirmed that the height of each step is the thickness of the monolayer, and knowing where the monolayer area and the vacuum area are, the number of layers in all areas can be counted starting from the vacuum and the monolayer and going up one by one.

**Figure 22(e)** is a graph showing the number of layers and intensities corresponding to each flat area in **Figure 22(c)** including the standard deviation. All four graphs do not fit perfectly, which is presumed to be the deviation caused by bending or tilting the

specimen. Instead of comparing the number of layers by an intensity jump with adjacent areas, the range in which the number of layers can be verified using absolute intensity values in all areas is up to the bilayer.

The number of layers determined in each area is colored in **Figure 22(b)**. Each color corresponds to the number of layers and is indicated in the legend on the right. Two features can be identified in the image. There is a linear defect extending straight from the center of the spiral WSe<sub>2</sub> to the lower right corner, and a linear defect extending zigzag from the center to the upper left corner.

The number of layers on the left and right of the line defect formed in the lower right direction does not change with the center of the line defect. That is, it can be seen that the defect is not accompanied by an increase or decrease in thickness like the extra half plane, but is formed for other reasons.

A zigzag line defect formed in the upper left direction shows to be one layer thicker when going from right to left. This corresponds to the shape of the red dotted line shown in **Figure 11(b)**. When a spiral structure is formed as one half plane climbs up another half plane, the covered edge inside the triangular structure does not grow anymore, but the exposed edge portion of the triangular edge grows, forming a zigzag-shaped extra half plane<sup>[9]</sup>. In other words, it can be inferred that this line defect is caused by the extra half plane of the bottom layer having a bumpy edge.



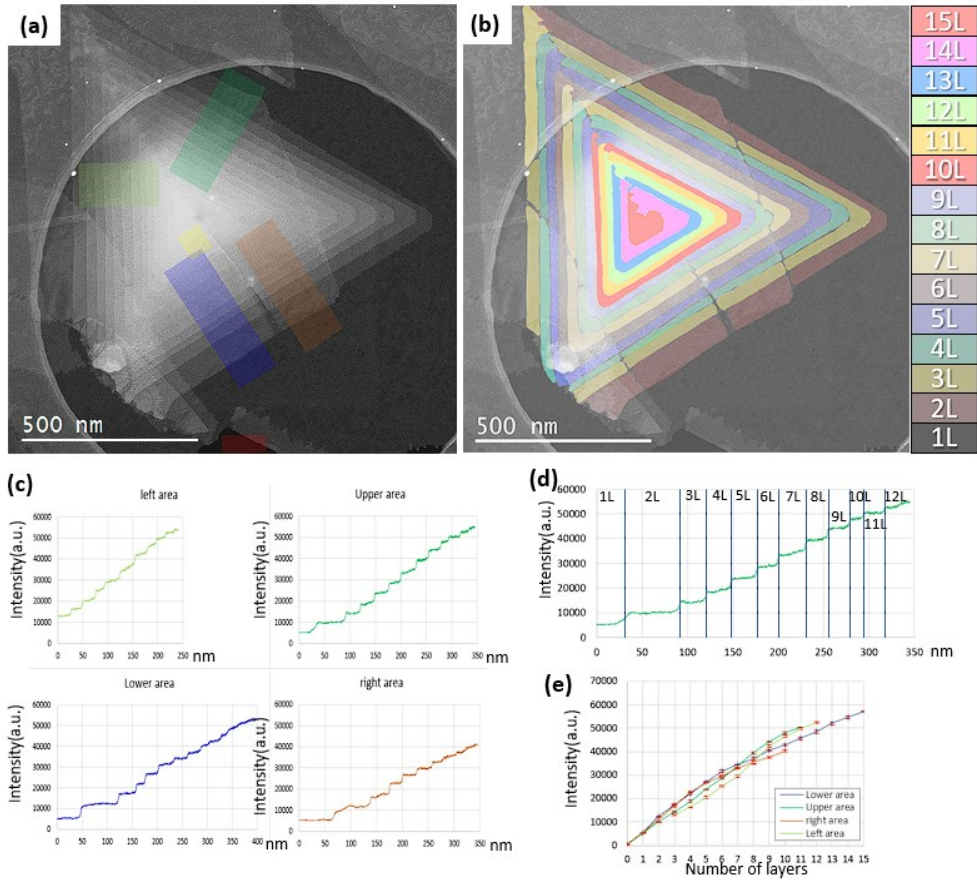


**Figure 22.** (a) HAADF image of spiral WSe<sub>2</sub> with a colored box for which the line profile is analyzed. (b) HAADF image colored with the color corresponding to the number of layers. Legend is located on the right side. (c) Line profiles in each area colored in (a). (d) Line profile showing the number of layers in each region in the region marked in green in (a). (e) A graph summarizing intensities for each number of layers for each region in (c).

In **Figure 23(a)**, four regions having different features are classified, and the diffraction patterns of each region are shown in **Figure 23(b–e)**. The region (b) is a flat, and uniform spiral WSe<sub>2</sub>. The region (c) is a region where the spiral WSe<sub>2</sub> is greatly bent because it lies with the edge of the grid carbon hole. And the overlapped region is in contact with the rough carbon surface. The region (d) is the area where the WSe<sub>2</sub> of the bottom layer is twisted and a moire pattern appears. The region (e) is an another area where moire patterns formed. Areas (c), (d), and (e) are complex systems, so in this study, analysis is performed in area (b), which is a uniform and simple area.

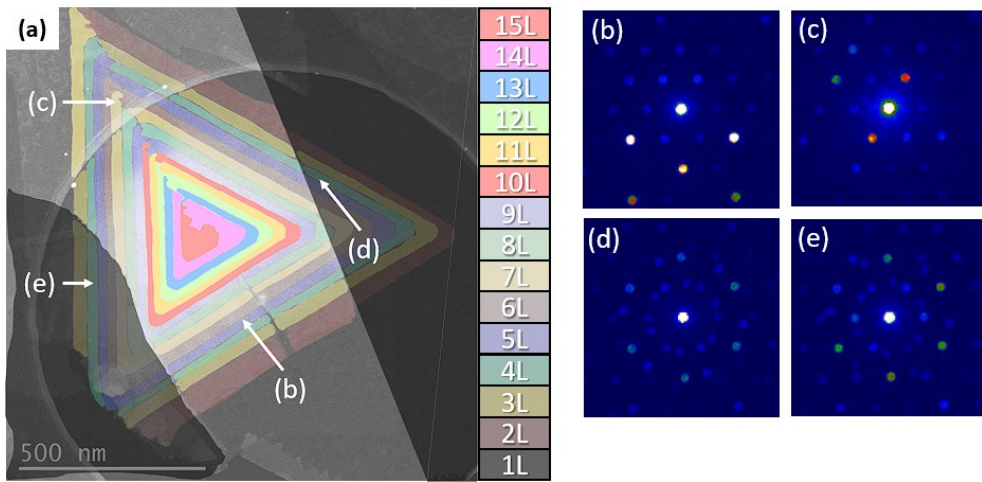


**Figure 23.** (a) HAADF image of WSe<sub>2</sub> spiral with the number of layer determined.(b–d) Representative diffraction pattern of 4 representative region indicated in (a). Each region corresponds to (b)uniform stacked region, (c)uniform stacked region with carbon grid, (d)Moire region due to the twist of the bottom layer, (e)another Moire region.

### 3.1.2. Determination of the type of dislocation

**Figure 24** represents the measured 4D-STEM data. Here, we analyze line defect or topological defect extending straight down to the right from the threading dislocation at the center of the spiral WSe<sub>2</sub>.

**Figure 24(a)** shows the vADF image, and **Figure 24(c-e)** shows the vDF image for each diffraction point shown in diffraction pattern of **Figure 24(b)**. Here, looking at the vDF image for  $\mathbf{g}_2 = (10-10)$ , **Figure 24(d)**, it can be observed that the contrast of the line defect disappears in the bilayer region, which is indicated by a red arrow.

In Section 1.3.3., it was mentioned that the contrast occurs when the dot product of  $\mathbf{g}$  and the displacement field,  $\mathbf{R}$ , is not zero<sup>[18]</sup>. Simply put, if the Burgers vector,  $\mathbf{b}$ , and  $\mathbf{g}$  are perpendicular, the dot product equals 0,  $\mathbf{g} \cdot \mathbf{b} = 0$ , and the contrast disappears. Through the contrast of **Figure 24(c-e)**, it can be determined that atomic positions of this topological defect is not displaced from the lattice point of the perfect crystal in the  $[10-10]$  ( $=\mathbf{g}_2$ ) direction, and all displacements can be occurred in the  $[1-210]$  direction.

In the following section, we will show that this defect has the character of a edge dislocation and confirm the Burgers vector. Therefore, the expressions of edge dislocation and Burgers vector were used in the **Figure 24** in advance.

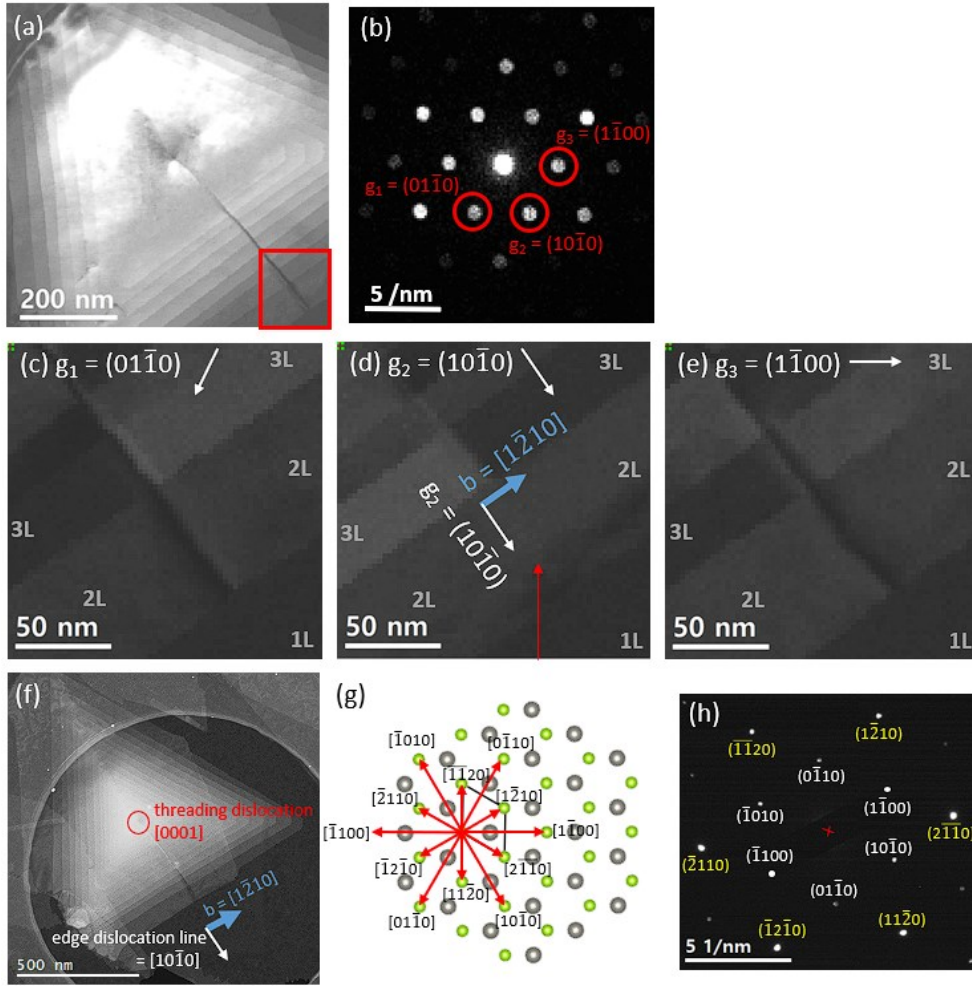


**Figure 24.** (a–e) Visualized 4D–STEM data. (a) vADF image, (b) diffraction pattern at the top left corner position of the red box in (a), (c–e) vDF images of the red box area for the three  $\mathbf{g}$  vectors shown in (b). In (d) with  $\mathbf{g}_2$  selected, it can be observed that the contrast disappears in the bilayer region indicated by the red arrow. (f) HAADF image with dislocation information displayed, (g) c–axis direction view of monolayer WSe<sub>2</sub>. The  $\langle 1-210 \rangle$  direction family and the  $\langle 10-10 \rangle$  direction family are indicated by red arrows. (h) Acquired selected area electron diffraction pattern of WSe<sub>2</sub> in other microscope (JEM 2100F). The first order diffraction spot  $\{10-10\}$

is expressed in white letters, and the second order diffraction spot  $\{1-210\}$  is expressed in yellow letters. It is an image so that readers can refer to the relationship between each direction.

### 3.1.3. Atomic resolution analysis of dislocation in bilayer WSe<sub>2</sub>

Spiral WSe<sub>2</sub> layers grow in parallel after the moment they start growing, but there is no reason for them to be parallel to the plane that was already stacked before spiral growth took place. In the case of the spiral WSe<sub>2</sub> analyzed here, one layer at the bottom has an antiparallel relationship with the spiral WSe<sub>2</sub>. Accordingly, the bilayer region composed of the bottom layer and the first layer from which the spiral TMD grows is as shown in **Figure 20(d)**. It has a 2H structure.

**Figure 25(a)** is an HAADF image of the white box area of **Figure 20(c)**, which is a bilayer region. This is an enlarged image of the line defect extending in a straight line defect formed in the lower right direction mentioned above. In the monolayer area where the line defect ends, an intact monolayer is confirmed without tearing or overlapping, as shown in the lower right side of **Figure 25(b)**.

Interlayer interactions in van der Waals materials are significantly smaller than intralayer interactions. In the monolayer area, the continuous bottom surface is not greatly affected by how the second layer is placed, so it exists continuously without being

torn or overlapped. From this, it can be inferred that the line defect appearing in the bilayer region is a pattern caused by the overlapping of the bottom layer and the top layer.

The red boxed area in **Figure 25(a)** is enlarged and shown in **Figure 25(c)**. Two unbroken layers overlap to make this pattern, and as shown above, the component of the displacement field,  $\mathbf{R}$ , in the vertical direction,  $[10-10]$ , is zero, so it can be seen that deformation occurred only in the horizontal direction,  $[1-210]$ . The horizontal lattice constant,  $\mathbf{a}$ , of the monolayer region was observed to be greater than that of the bilayer region. From this, it can be inferred that the second layer is more densely arranged than the bottom layer along the  $[1-210]$  direction.

By contracting the horizontal lattice constant of the second layer, a model was created so that 26 unit cells in the lower layer and 27 unit cells in the upper layer overlapped, and shown in **Figure 25(d)**. It can be seen that the position of the atoms in the overlapping area matches the position of the atoms shown in **Figure 25(c)**.

**Figure 25(e)** shows the result of HAADF image simulation with a two layer superlattice model in **Figure 25(d)** made by multiplying the horizontal lattice constant of the upper layer by 26/27. It can be observed that this image is also similar to the HAADF image of **Figure 25(c)** measured in the experiment. This structural model is similar to the edge dislocation with one additional unit cell on the upper layer. Here, these topological defects formed in the bilayer will be referred to as dislocations or edge dislocations.



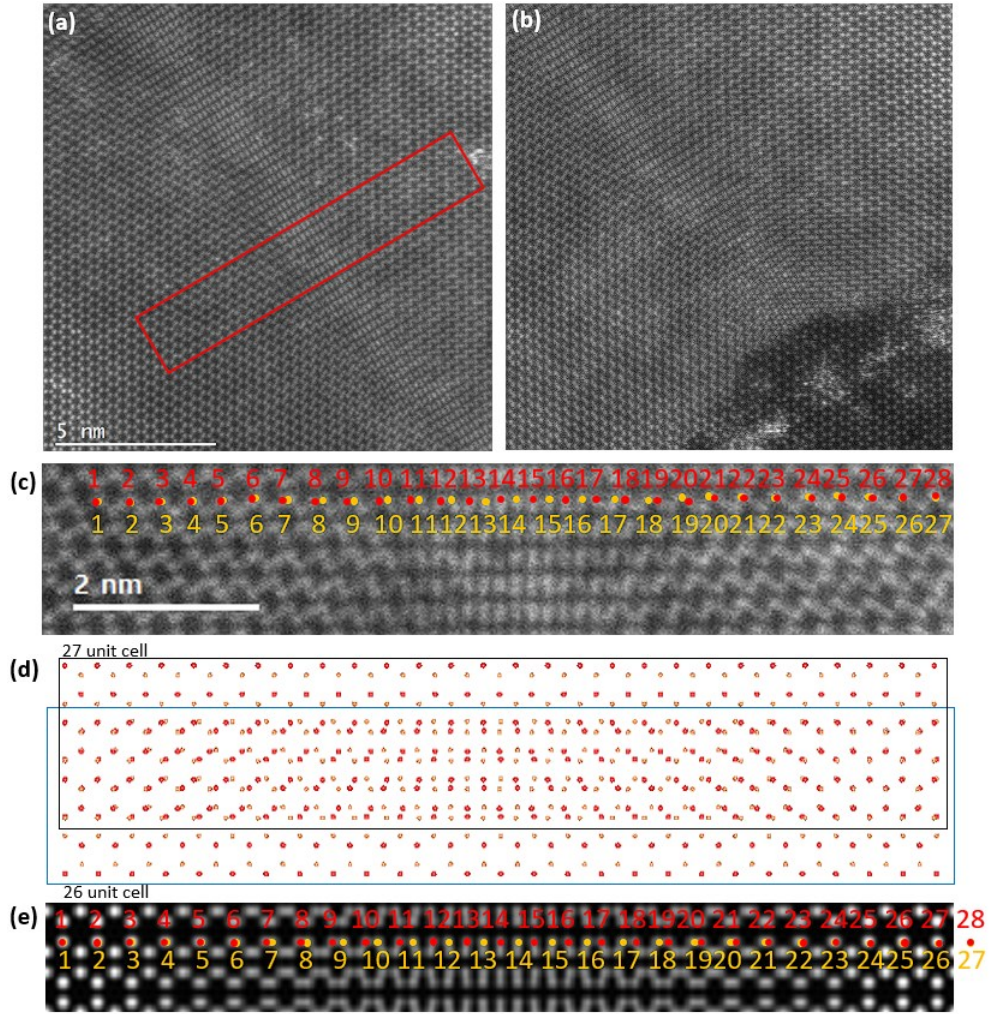


**Figure 25.** (a) HAADF image of the white boxed area of **Figure 20(c)**, which is the bilayer region. (b) HAADF image of the blue boxed area in **Figure 20(c)**. In the monolayer area where the line defect ends, an intact monolayer is observed without tearing or overlapping. (c) An enlarged image of the red boxed area in (a) showing the position of each atom. Atomic positions with a short period are shown in red, and atomic positions with a long period are shown in yellow. (d) A model in which 26 unit cells (bottom) and 27 unit cells (top) are partially overlapped for the width of  $26a$ , and  $a$  is a unit cell vector. The arrangement of the atomic positions is

similar as shown in (c). (e) Image obtained by HAADF simulation of a bilayer structure with 26 unit lattices for the lower layer and 27 unit lattices for the upper layer. The image is similar to (c).

In the proposed model, we will find the Burgers vector of the dislocation. In **Figure 26(c, d)**, the crystal directions and plane directions are indicated. Also, the  $c$ -axis view and the  $[10-10]$  direction view are shown in **Figure 26(a, b)**. The Burgers circuit of this model is a counterclockwise circuit that goes and returns by 27 unit cells in the  $[1-210]$  direction and by 1 unit cell in the  $[0001]$  direction. The Burgers vector obtained at this time is  $1/3[1-210]$ . The dislocation direction is the  $[10-10]$  direction and is perpendicular to the Burgers vector, so it is an edge dislocation.

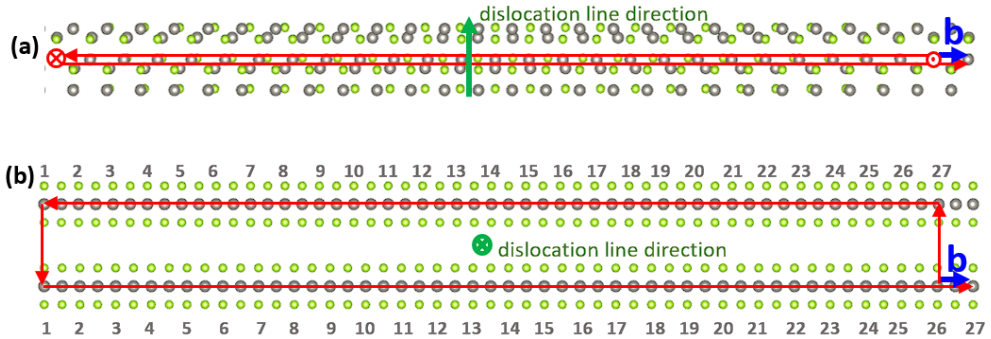


**Figure 26.** Burgers circuit (red arrow), Burgers vector (blue arrow), and dislocation line directions (green arrow) for the proposed model; (a)  $c$ -axis direction view, (b)  $[10-10]$  direction view.



To explain further, it can be seen that the line defect contrast does not disappear in any vDF image of **Figure 24** from the trilayer region and thicker region. From this, it can be inferred that displacement in a different direction from  $\mathbf{b} = [1-210]$  has occurred since the third layer. From the third layer, it is discussed that they are stacked parallel to the lower layer, and to have stable stacking on both sides of the line defect, displacement in the  $[10-10]$  direction would occur as shown in **Figure 15(a)**. Even in the vDF image in **Figure 24(d)**,  $\mathbf{g} = (10-10)$ , the contrast appears because there is displacement in the corresponding direction from the third layer, even though the image in which the contrast due to the dislocation of the bottom bilayer disappears.

#### 3.1.4. Formulation of dislocation energy in van der Waals bilayer structure

In **Figure 27**, it can be seen that the edge dislocation appearing in the bilayer spreads over a wide area. In the case of three-dimensional materials, the strain field of dislocation is known to be at the level of  $2 \text{ nm}^{[25]}$ . But the dislocation in the bilayer region is  $17.7 \text{ nm}$  when the FWHM of HAADF intensity is measured, confirming that the strain field is distributed over a much wider area.

To explain why this is the case, the interlayer interaction energy and the strain energy within the layer must be considered together. While one additional unit cell spreads over the wide

strained region for 2H bilayer, the stacking between the two layers becomes AA' stacking, then SP stacking, and then AA' stacking again, as shown in **Figure 27(c)**. The approximate energy for this process is shown in the graph and can be calculated<sup>[17]</sup>.

In order to see the rough trend, let's approximate that the interlayer interaction energy in a wide strain field region has the average value of AA' and SP on average. Then, the interlayer interaction energy has a value proportional to the width of the strain field region ( $E_{vdW}=Bn$ , dislocation is dispersed into  $n$  lattices). That is, the interplanar interaction becomes more stable as the width of the strain field becomes narrower.

Consider the strain energy in the layer formed by the contraction of the layer. Assuming that the deformation behavior follows the generalized Hooke's law ( $F=-kx$ ) under non-extreme deformation conditions, the deformation energy is proportional to the square of the deformation ( $U=0.5kx^2$ ). It can be seen in **Figure 27(d)** that it is 10 times more stable when 10 unit cells relax a divided strain of 0.01 than when one unit cell relaxes all strains of 0.1.

In other words, as the width of the strain field widens, it becomes more stable because more unit cells divide and relax the same strain, and this energy is inversely proportional to the number  $n$  of unit cells included in the width of the strain field ( $E_{strain}=A/n$ ).

The total energy of the edge dislocation should consider the above two effects together ( $E_{disl}=E_{strain}+E_{vdW}$ ). As the width increases, the interlayer interaction becomes unstable and the

strain energy in the layer becomes stable, so an appropriate balance point exists. The width of the most stable dislocation can be obtained by differentiating the total energy with respect to  $n$ . This is summarized in the formula below.

$$E_{disl} = E_{strain} + E_{van\ der\ Waals}$$

$$E_{disl} = \frac{A}{n} + Bn$$

$$\frac{dE_{disl}}{dn} = 0 = -\frac{A}{n^2} + B$$

$$n_{stable} = \sqrt{A/B}$$

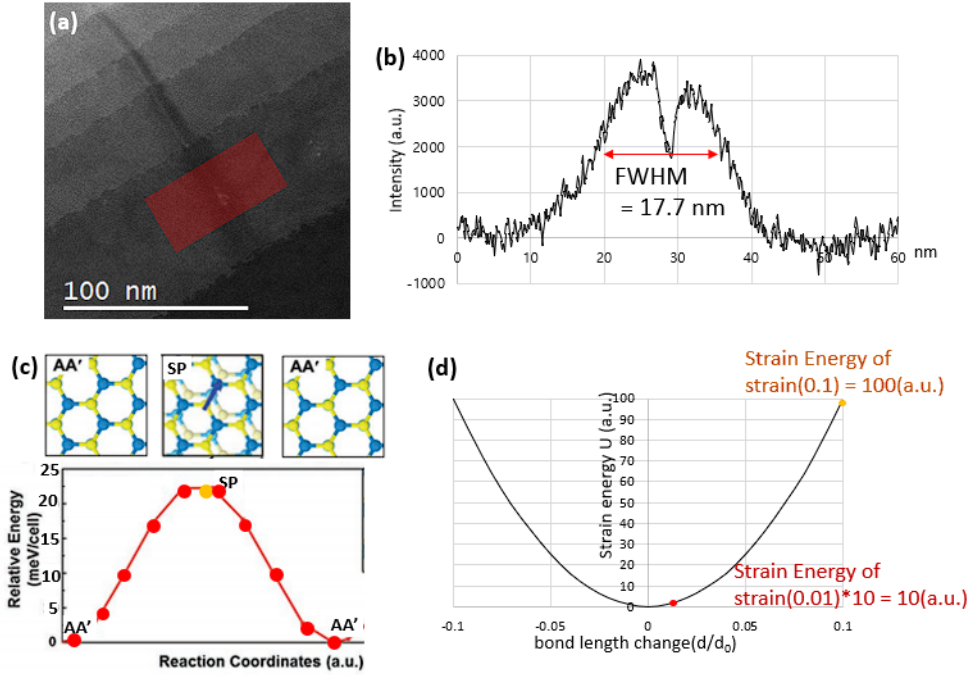


**Figure 27.** (a) HAADF image in bilayer dislocation region. (b) Line profile of the HAADF intensity profile in the red region in (a) multiplied by  $-1$ . (c) Interplanar interaction energy change graph during the bilayer 2H stacking change process. (d) Graph of strain energy according to strain.

## 3.2. Determination of stacking order of multi layered WSe<sub>2</sub>

### 3.2.1. Bilayer binding energy of WSe<sub>2</sub> and possible candidates for a stacking sequence in spiral WSe<sub>2</sub>

In this section, we explore methods to analyze the arrangement of atoms in regions of three or more layers. **Figure 28** summarizes how to extract possible stacking sequences. There are six ways in which the two layers can be stacked, as shown in **Figure 28(c)**. There are three cases of antiparallel stacking on the left side and three cases of parallel stacking on the right side. The energy calculation results for each stacking are shown in **Figure 28(b)**. In the case of the spiral WSe<sub>2</sub>, all layers are stacked in parallel, so it can be seen that only the AB or AC stacking indicated by the red box can be a candidate.

Consider the stacking sequence of the trilayer region in **Figure 28(a)**. First of all, since the bottom layer is maintained and another stacking is placed on top, we know that the bottom two layers are A'A stacking. In other words, how the third layer is stacked is only thing to find out.

The third layer only needs to be B or C, not A. Also, since the intensities of the left and right sides are different in the vDF image of **Figure 24**, it can be inferred that the stacking of the left and right sides is not the same. That is, it can be seen that one side of the trilayer region is A'AB stacking and the other side is A'AC stacking.

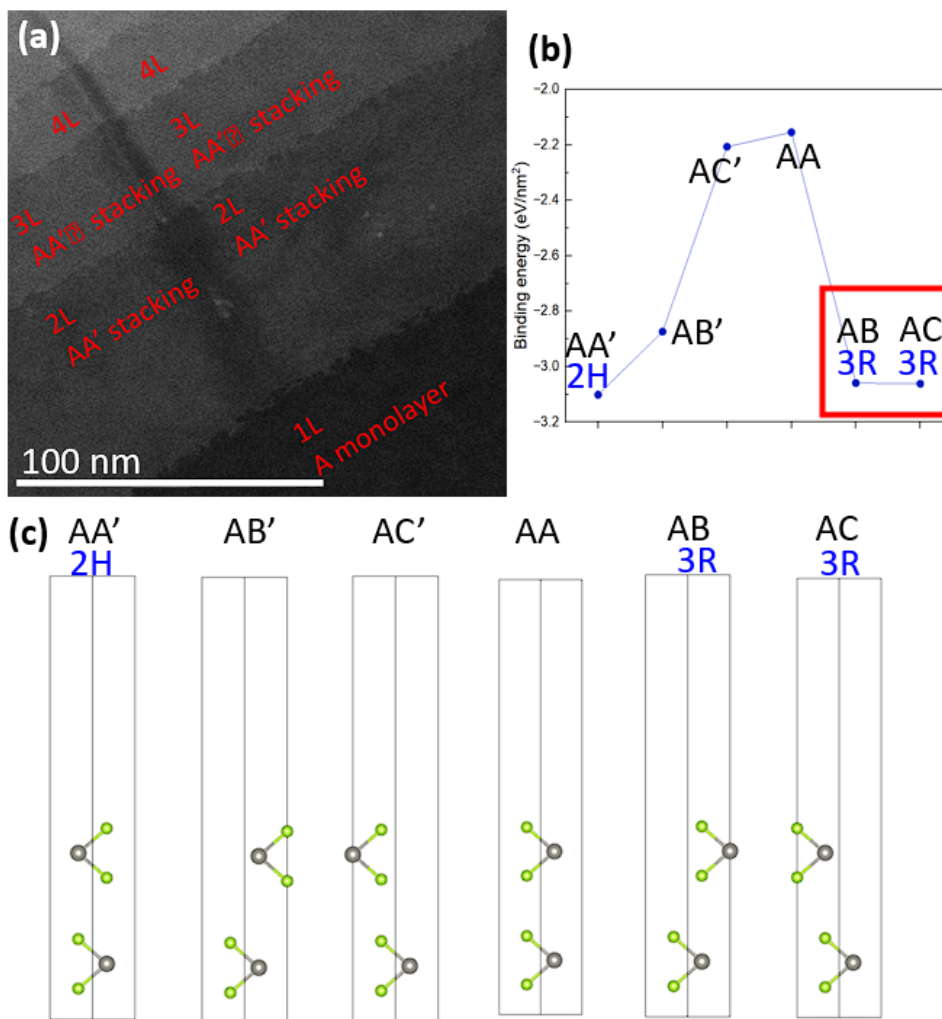


**Figure 28.** (a) HAADF image showing possible stacking sequences. (b) Calculation result of binding energies in 6 possible bilayer stackings. (c) The structure of the 6 possible bilayer stacking.

### 3.2.2. PACBED simulation for various stacking sequence of multilayer WSe<sub>2</sub>

As shown in **Figure 24**, 4D-STEM data can play an important role in analyzing stacking sequence. Since there is a difference in diffraction patterns depending on how the stacking is performed, the stacking sequence in each domain can be determined by analyzing the diffraction pattern of each region observed in the experiment.

In order to compare the diffraction patterns measured in the experiment, simulations were performed on the diffraction patterns for each stacking sequence listed in **Figure 29**. A simulated example diffraction pattern is inserted at the top right of **Figure 29**.

The diffraction pattern of the monolayer TMD material basically shows a 3-fold symmetry with inversion symmetry broken<sup>[26]</sup>. That is, the intensity of one side of the center beam is greater than that of the opposite side. This phenomenon can be expressed with a parameter called polarity,  $P$ . Since the 3-fold symmetry of the material is preserved when atoms are located only at the A, B, and C sites, the first order diffraction spots can be classified as two groups. P1, P3, P5 and P2, P4, P6.

**Figure 29** is a bar graph showing the intensity of each diffraction point according to the stacking sequence. As mentioned above, P1, P3, and P5 have the same intensity, and P2, P4, and P6 have the same intensity, but you can see that the two sets have different intensities. In this study, the value representing polarity is defined as  $P = (P1+P3+P5)-(P2+P4+P6)$ , and the average

intensity of the six diffraction points  $Avg = (P1+P2+P3+P4+P5+P6)/6$  was defined and analysis was performed.

The stacking sequence simulated is only A'AB and A'AC stacking for trilayer structure which was selected above. If it is thicker than trilayer, it is arbitrarily set and stacked in a direction satisfying the 3R structure. In the case of A'AB, they were stacked sequentially in ABCABC... order, and in the case of A'AC, in ACBACB... order.

The average intensity for each stacking sequence is shown in **Figure 30**. The intensity repeated periodically every three layers. In **Figure 30(a)**, it can be seen that the average intensity periodically disappears whenever one cycle of ABC or ACB is completed, and this is marked with a red box.

This feature is due to the structural characteristics of the ABC trilayer structure. When each layer is stacked at three different sites, such as ABC, the atomic columns at the A site, B site, and C site all have one tungsten atom and two selenium atoms.

Let's assume that the Z-direction position of atoms does not significantly affect the image with assuming that the channeling effect, etc., is insignificant. When electrons are passed through the sample and the projection is seen, the image changes from a monolayer honeycomb structure with three lattice points to an ABC trilayer two dimensional hexagonal closest dense structure, and the unit lattice becomes smaller and has only one lattice point.

As a result, a large interplanar distance corresponding to the

first order diffraction spot is prohibited. That is, the first order diffraction spot hardly appears in the ABC trilayer structure. If another layer is stacked on top of it to form an ABCA 4-layer structure, the first order electron diffraction spot shows only the effect of the A layer excluding the effect of ABC. However, in an actual experiment, since the HAADF intensity is affected by the electron channeling effect, etc., the thicker the thickness, the more factors should be considered.

Next, how the average intensity changes according to the tilt of the sample is shown in **Figure 30(b)**. It can be confirmed that up to a tilt of 10 mrad, regardless of the azimuth angle, a robust periodic behavior is exhibited up to a thickness of 15 layers. If a well controlled experiment is performed, it is not difficult to achieve with an error within 10 mrad if the zone axis is aligned, and if the actual sample has a 3R structure, it can be expected that it should show a periodicity of 3 layers.

**Figure 31** shows the polarity according to each stacking sequence. **Figure 31(a)** shows the polarity values at zero tilt, but no clear trend is noticeable. However, as shown in **Figure 31(b)**, when stacking in the ABCABC... order and stacking in the ACBACB... order are classified separately, former group shows an overall negative sign and the latter group shows an overall positive sign in the area where the tilt is 10 mrad or more. It can be observed that the polarity changes according to the stacking sequence. However, if the tilt value in the experimental situation cannot be accurately determined due to the high tilt sensitivity, interpretation may be hard.



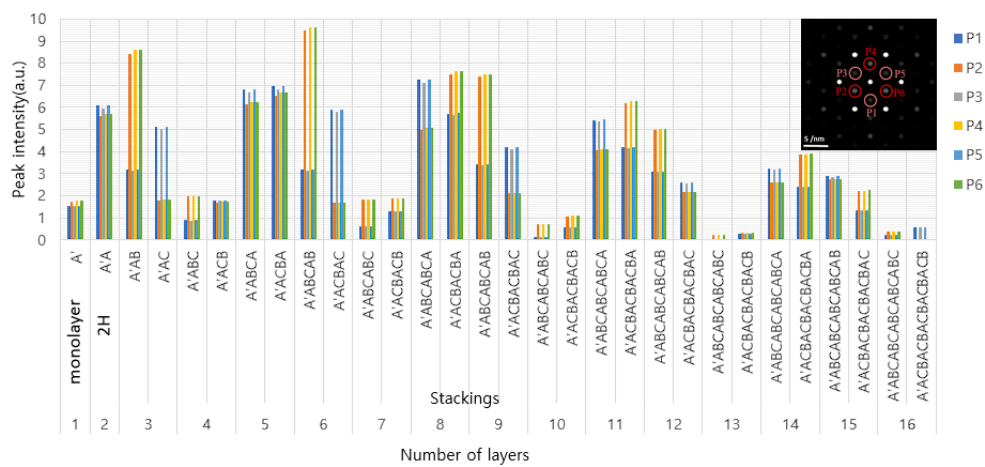


**Figure 29.** Intensity graph of 6 first order diffraction spots according to each stacking sequence. The inset image displays a representative diffraction pattern and the index of each diffraction spot.

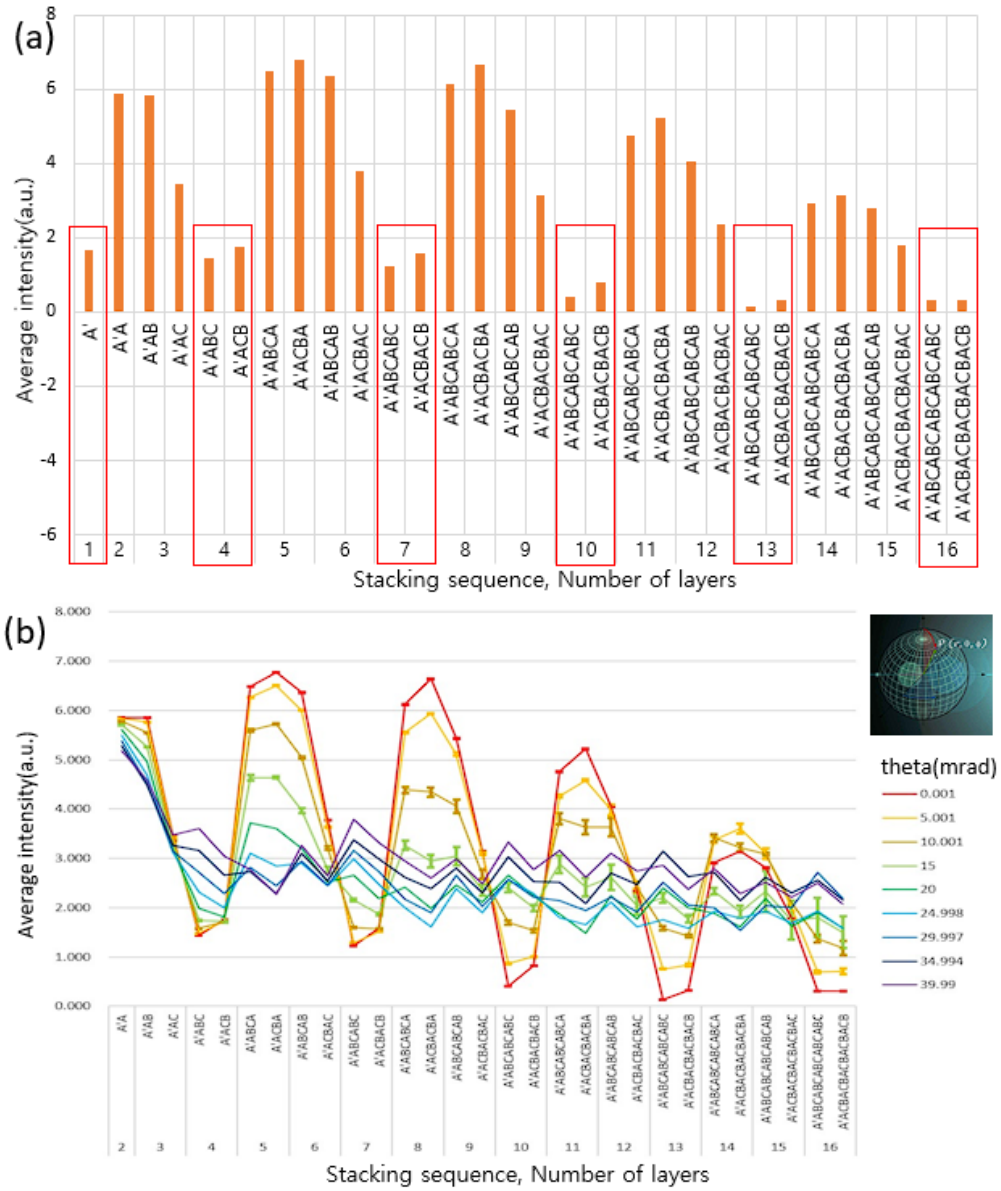


**Figure 30.** Average intensity graph of simulated diffraction patterns according to the stacking sequence. (a) Zone axis condition with no tilt, (b) superimposed graph for each tilt angle,  $\theta$ , shown in legend. effect according to azimuth,  $\phi$ , is expressed as standard deviation at each theta point.

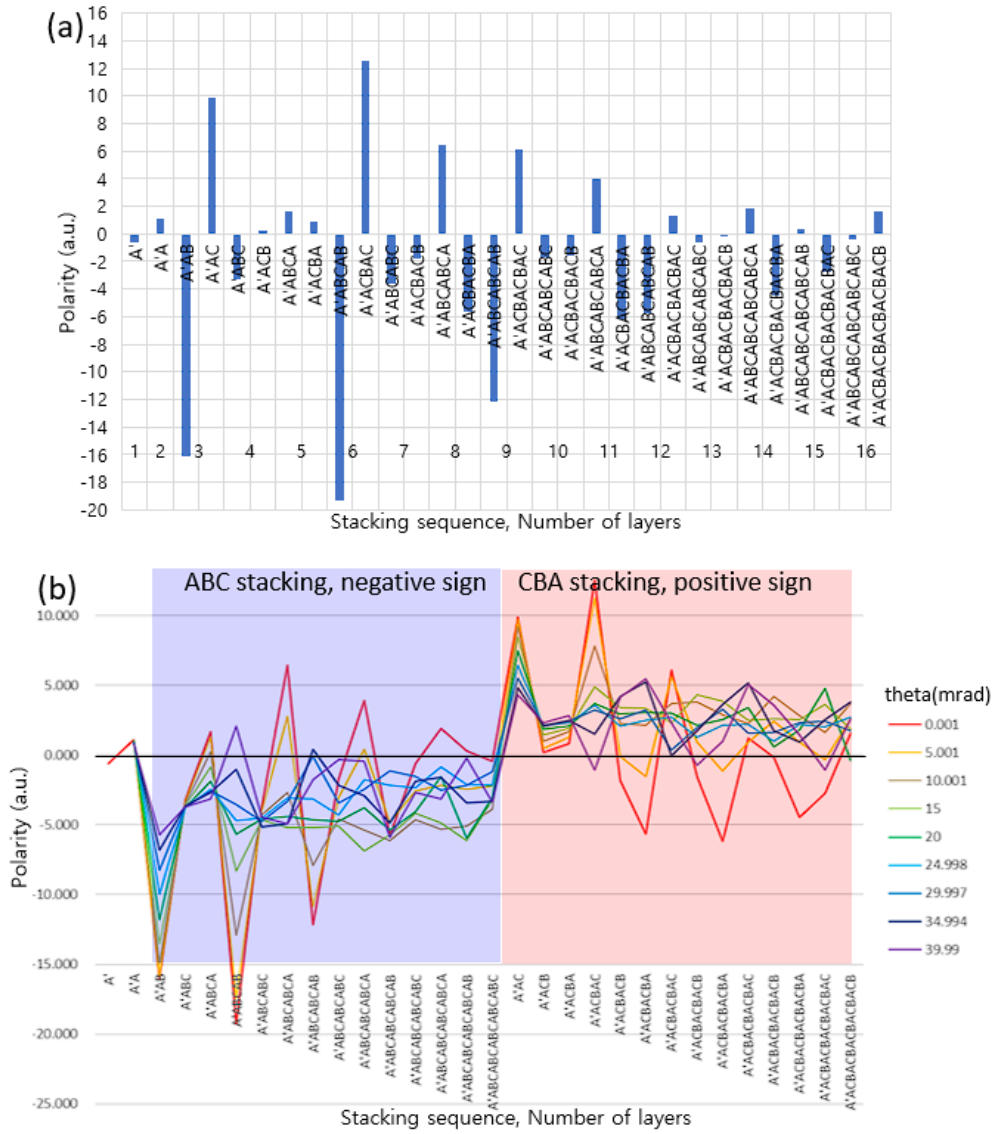


**Figure 31.** Polarity graph of simulated diffraction patterns according to the stacking sequence. (a) Zone axis condition with no tilt, (b) superimposed graph for each tilt angle,  $\theta$ , shown in legend. effect according to azimuth,  $\phi$ , is expressed as standard deviation at each theta point.

### 3.2.3. Experimental 4D–STEM image of spiral WSe<sub>2</sub>

**Figure 32** is the average intensity and polarity map reconstructed from the measured 4D–STEM data. Looking at the average intensity in **Figure 32(a)**, the right side of the line defect shows that it darkens every 3 layers. However, the left side shows a slightly changing behavior at moderate intensity. Through this, it can be inferred that the right region is close to the 3R structure of the 3 layer period. Conversely, the area on the left is stacked likewise with all sides parallel, but it can be inferred that it is stacked in a different stacking than the ABCABC... stacking.

Looking at the polarity of **Figure 32(b)**, it can be observed that the left side of the line defect shows positive polarity and the right side shows negative polarity. This characteristic is maximized in the upper left side of the spiral where the sample is curved a lot, and the size is small and sign alternates in the lower right corner where the zone axes are almost aligned.

Since the number of possible stacking sequences up to 15 layers is enormous, it is not easy to say how each sides are stacked. However, the sign of the polarity is clearly changing through the line defect, and further research will be able to analyze the effect of the line defect on stacking.

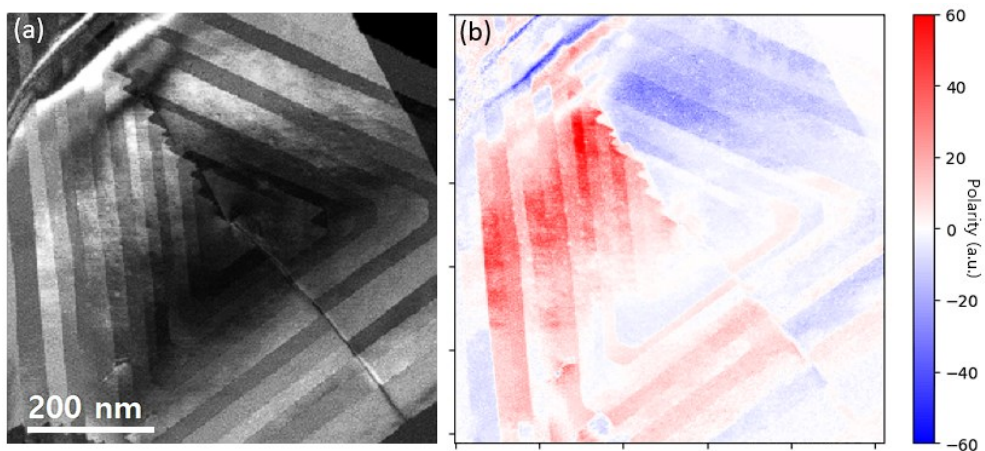


**Figure 32.** Reconstructed 4D-STEM image of (a) average intensities and (b) polarity of the first order diffraction peak.

## Chapter 4. Conclusions

Van der Waals materials have high utility value thanks to their physical properties and processability, and are a field that is being actively researched. Spiral TMDs also show value for device applications and can be used as nano sized inductors or active electrodes.

In this paper, spiral WSe<sub>2</sub> was investigated using a transmission electron microscope. The formation of edge dislocations in bilayer region of van der Waals materials was analyzed by observing the bilayer region of line defects across the spiral WSe<sub>2</sub>. Unlike three dimensional materials that confine dislocations in a small area of about 2 nm, dislocations in two dimensional materials spread over a wide area to lower energy. These dislocations may have high mobility, but in this case dislocation entangled with threading dislocations at the center of the spiral WSe<sub>2</sub> and remain fixed in the same position. Cases in which line defects formed in two dimensional materials are analyzed are rare, and it is expected that it will be helpful in investigating the effect of defects in future device applications of van der Waals materials.

And through 4D-STEM measurement and diffraction pattern simulation, we analyzed how diffraction patterns appear in various stacking sequences. For the diffraction pattern, the first-order diffraction peak, which is less affected by thickness, was used, and two parameters, average intensity and polarity, were extracted and

analyzed. In the case of the 3R structure, it was confirmed that the average intensity rapidly darkens with a cycle of three layers. It was judged that polarity tended to favor positive or negative numbers according to stacking conditions, but a specific stacking sequence could not be determined. Through rigorous research and analysis in the future, it will be possible to conduct research to find out the stacking sequence layer by layer through average intensity and polarity analysis.

## Bibliography

- [1] Geim, Andre K., and Irina V. Grigorieva. "Van der Waals heterostructures." *Nature* 499.7459 (2013): 419–425.
- [2] Choudhury, Tanushree H., et al. "Epitaxial growth of two-dimensional layered transition metal dichalcogenides." *Annual Review of Materials Research* 50 (2020): 155–177.
- [3] Chen, Liang, et al. "Screw-dislocation-driven growth of two-dimensional few-layer and pyramid-like WSe<sub>2</sub> by sulfur-assisted chemical vapor deposition." *Acs Nano* 8.11 (2014): 11543–11551.
- [4] Zhang, Liming, et al. "Three-dimensional spirals of atomic layered MoS<sub>2</sub>." *Nano letters* 14.11 (2014): 6418–6423.
- [5] Ly, Thuc Hue, et al. "Vertically conductive MoS<sub>2</sub> spiral pyramid." *Advanced Materials* 28.35 (2016): 7723–7728.
- [6] Sarma, Prasad V., et al. "Electrocatalysis on edge-rich spiral WS<sub>2</sub> for hydrogen evolution." *ACS nano* 13.9 (2019): 10448–10455.
- [7] Strachan, Jyah, Anthony F. Masters, and Thomas Maschmeyer. "3R-MoS<sub>2</sub> in review: History, status, and outlook." *ACS Applied Energy Materials* 4.8 (2021): 7405–7418.
- [8] Chen, Liang, et al. "Screw-dislocation-driven growth of two-dimensional few-layer and pyramid-like WSe<sub>2</sub> by sulfur-assisted chemical vapor deposition." *Acs Nano* 8.11 (2014): 11543–11551.
- [9] Fan, Xiaopeng, et al. "Controllable growth and formation mechanisms of dislocated WS<sub>2</sub> spirals." *Nano letters* 18.6 (2018): 3885–3892.



- [10] Sarma, Prasad V., et al. "Electrocatalysis on edge-rich spiral WS<sub>2</sub> for hydrogen evolution." *ACS nano* 13.9 (2019): 10448–10455.
- [11] Qiu, S. Roger. "Crystal Growth for Beginners. Fundamentals of Nucleation, Crystal Growth and Epitaxy" *Acta Crystallographica. Section B, Structural Science, Crystal Engineering and Materials* (2019).
- [12] Yankovich, Andrew B., et al. "Picometre-precision analysis of scanning transmission electron microscopy images of platinum nanocatalysts." *Nature communications* 5.1 (2014): 4155.
- [13] Lee, Z., et al. "Optimum HRTEM image contrast at 20 kV and 80 kV-exemplified by graphene." *Ultramicroscopy* 112.1 (2012): 39–46.
- [14] Ngome Okello, Odongo Francis, et al. "Atomic-level defect modulation and characterization methods in 2D materials." *APL Materials* 9.10 (2021): 100902.
- [15] Zhao, Xiaoxu, et al. "Differentiating polymorphs in molybdenum disulfide via electron microscopy." *Advanced Materials* 30.47 (2018): 1802397.
- [16] Kim, Cheol-Joo, et al. "Stacking order dependent second harmonic generation and topological defects in h-BN bilayers." *Nano letters* 13.11 (2013): 5660–5665.
- [17] Kim, Jung Hwa, et al. "Interface-Driven Partial Dislocation Formation in 2D Heterostructures." *Advanced Materials* 31.15 (2019): 1807486.
- [18] Williams, David B., et al. *The transmission electron microscope*. Springer Us, 1996.

- [19] Eades, A. "Educational article: when to use selected-area diffraction and when to use convergent-beam diffraction." *Acta Microscopica* 17.1 (2008): 101–105.
- [20] Mehta, Ankit Nalin, et al. "Unravelling stacking order in epitaxial bilayer MX<sub>2</sub> using 4D-STEM with unsupervised learning." *Nanotechnology* 31.44 (2020): 445702.
- [21] Ophus, Colin. "Four-dimensional scanning transmission electron microscopy (4D-STEM): From scanning nanodiffraction to ptychography and beyond." *Microscopy and Microanalysis* 25.3 (2019): 563–582.
- [22] Kim, Jung Han, et al. "Centimeter-scale green integration of layer-by-layer 2D TMD vdW heterostructures on arbitrary substrates by water-assisted layer transfer." *Scientific reports* 9.1 (2019): 1641.
- [23] Allen, Leslie J., and S. D. Findlay. "Modelling the inelastic scattering of fast electrons." *Ultramicroscopy* 151 (2015): 11–22.
- [24] Morin, Stephen A., et al. "Screw dislocation-driven growth of two-dimensional nanoplates." *Nano letters* 11.10 (2011): 4449–4455.
- [25] Liu, Quanlong, et al. "Strain field mapping of dislocations in a Ge/Si heterostructure." *Plos one* 8.4 (2013): e62672.
- [26] Deb, Pratiti, et al. "Imaging polarity in two dimensional materials by breaking Friedel's law." *Ultramicroscopy* 215 (2020): 113019.

## 국 문 초 록

나선형 이칼코겐화 전이금속은 초소형 유도기나 초소형 전극으로 응용될 수 있어 큰 관심을 받고 있다. 이 연구에서는 그 중 하나인 이셀레늄화 텅스텐( $\text{WSe}_2$ )을 투과전자현미경을 이용하여 분석한다. 반데르발스 물질의 결함을 확인하고 적층 방식을 분석하는 기법을 제시하였다. 반데르발스 물질을 공학적으로 이용할 때 소자 열화의 원인 분석에 도움이 될 것이다.

나선형  $\text{WSe}_2$ 는 중심에 나선전위를 형성하며 하나의 면이 연속적으로 나선형으로 성장하여 피라미드 끝의 형태를 가진다. 나선형  $\text{WSe}_2$  결정의  $[0001]$  방향으로 존재하는 중심의 나선전위와  $[10-10]$  방향으로 존재하는 수평 방향의 칼날 전위에 얽힘이 일어나 칼날 전위가 한 위치에 고정되어 있어, 이 영역을 자세히 관찰할 수 있었다. 버거스 벡터와 회절 벡터의 내적이 0이 될 때 전위의 대비가 0이 된다는 점을 이용하여 전위의 버거스 벡터가  $[1-210]$  방향임을 확인하였다.

버거스 벡터의 크기를 분석하기 위하여 원자분해능 고각고리형암시야-주사투과전자현미경 이미지를 획득하였다. 그 결과 두 층 영역에서 위층이  $[1-210]$  방향으로 1개 단위격자만큼 수축하여 형성된 전위임을 확인하였고 버거스 벡터는  $1/3[1-210]$ 으로 판정되었다.

반데르발스 물질에서 이러한 전위는 면간 상호작용이 약하다는 특징 때문에 면 내부에 넓게 퍼져서 존재할 수 있다. 면간 쌓임의 엇갈림에 의해 불안정해지는 에너지와 변형장을 넓게 퍼뜨림으로써 안정화되는 에너지의 균형점을 찾음으로써 평형 전위 너비를 계산할 수 있다.

또한 각각의 주사 지점에서의 회절패턴을 이미지로 저장하는 4차원-주사투과전자현미경 이미지를 획득하였다. 가능한 적층 순서 중 3R 구조에 해당하는 적층 구조의 기울기별 회절패턴을 muSTEM 프로그램을 통해 시뮬레이션하였다. 회절 패턴에 적층 순서의 특징이 나타나는 두 가지 인자로 평균 세기와 극성을 정의하였다. 평균 세기는 두께가 15층 이하이고 시편의 기울기가 10 mrad 이하일 때, 3R 구조에서 3개 층을 주기로 급격히 어두워지는 모습이 나타남을 확인하였다. 극성은 적층 순서가 뒤집힐 경우 부호가 뒤집히는 현상을 보였다. 실험으로 측정된 회절패턴의 경우 칼날 전위를 기준으로 좌우의 극성의 부호가 뒤집히는 현상이 나타났다. 적층 순서가 뒤집히지 않더라도 극성의 부호가 뒤집히는 다른 이유가 있을 수 있기에 추가적인 연구가 필요하다.

**주요어** : 반데르발스 물질, 칼날전위, 적층, 투과전자현미경, 사차원-주사투과전자현미경

**학번** : 2019-26531